

Searching the InSight Seismic Data for Mars's Background-Free Oscillations

Cecilia Durán^{*1}, Amir Khan^{*1,2}, Johannes Kemper¹, Iris Fernandes³, Klaus Mosegaard³, Jeroen Tromp⁴, Marion Dugué¹, David Sollberger⁵, and Domenico Giardini¹

Abstract

Mars's atmosphere has theoretically been predicted to be strong enough to continuously excite Mars's background-free oscillations, potentially providing an independent means of verifying radial seismic body-wave models of Mars determined from marsquakes and meteorite impacts recorded during the Interior Exploration using Seismic Investigations, Geodesy, and Heat Transport (InSight) mission. To extract the background-free oscillations, we processed and analyzed the continuous seismic data, consisting of 966 Sols (a Sol is equivalent to a Martian day), collected by the Mars InSight mission using both automated and manual deglitching schemes to remove nonseismic disturbances. We then computed 1-Sol-long autocorrelations for the entire data set and stacked these to enhance any normal-mode peaks present in the spectrum. We find that while peaks in the stacked spectrum in the 2–4 mHz frequency band align with predictions based on seismic body-wave models and appear to be consistent across the different processing and stacking methods applied, unambiguous detection of atmosphere-induced free oscillations in the Martian seismic data nevertheless remains difficult. This possibly relates to the limited number of Sols of data that stack coherently and the continued presence of glitch-related signal that affects the seismic data across the normal-mode frequency range (~1–10 mHz). Improved deglitching schemes may allow for clearer detection and identification in the future.

Cite this article as Durán, C., A. Khan, J. Kemper, I. Fernandes, K. Mosegaard, J. Tromp, M. Dugué, D. Sollberger, and D. Giardini (2024). Searching the InSight Seismic Data for Mars's Background-Free Oscillations, *Seismol. Res. Lett.* **XX**, 1–17, doi: [10.1785/0220240167](https://doi.org/10.1785/0220240167).

[Supplemental Material](#)

Introduction

The Mars Interior Exploration using Seismic Investigations, Geodesy, and Heat Transport (InSight) mission has provided the first-ever detailed view of the interior structure of another planetary object besides the Earth and the Moon (e.g., Banerdt *et al.*, 2020; Lognonné, Banerdt, *et al.*, 2023), including its crust (e.g., Knapmeyer-Endrun *et al.*, 2021; Beghein *et al.*, 2022; Durán, Khan, Ceylan, Zenhäusern, *et al.*, 2022; Kim *et al.*, 2022), mantle (e.g., Khan *et al.*, 2021; Durán, Khan, Ceylan, Charalambous, *et al.*, 2022; Huang *et al.*, 2022), core (e.g., Stähler *et al.*, 2021; Wang and Tkalčić, 2022; Irving *et al.*, 2023; Khan *et al.*, 2023; Le Maistre *et al.*, 2023; Samuel *et al.*, 2023), seismicity (e.g., Giardini *et al.*, 2020; Stähler *et al.*, 2022), and bulk composition (e.g., Khan *et al.*, 2022), among others.

These studies have largely relied on the observation of body waves from the highest-quality marsquakes and two imaged meteorite impacts. With the exception of the two impacts (Horleston *et al.*, 2022; Posiolova *et al.*, 2022), most of the located events originated within the Cerberus Fossae graben system ~30°–40° due at east of the station (e.g., Drilleau *et al.*, 2022; Durán, Khan, Ceylan, Charalambous, *et al.*, 2022; Zenhäusern *et al.*, 2022; Wang *et al.*, 2023), resulting in a relatively limited

spatial sampling and a potential northern hemispherical bias in our view of the planet.

In contrast to short-period body waves, the use of the long-period seismic response of a planet to excitation in the form of normal modes is advantageous in that the free oscillation frequencies are independent of the source mechanism such that epicenter location and origin time are not required for determining the average radial seismic structure of a planet as demonstrated with the Preliminary Reference Earth Model (PREM) (Dziewonski and Anderson, 1981). Consequently, the observation of normal modes on Mars would serve as an important diagnostic tool with which the Martian seismic body-wave models could be independently verified.

1. Institute of Geophysics, ETH Zurich, Zurich, Switzerland, <https://orcid.org/0000-0003-4269-930X> (CD); <https://orcid.org/0000-0002-7787-4836> (AK); <https://orcid.org/0000-0003-1841-9590> (JK); <https://orcid.org/0000-0001-9188-8321> (MD); <https://orcid.org/0000-0002-5573-7638> (DG); 2. Institute of Geochemistry and Petrology, ETH Zurich, Zurich, Switzerland; 3. Niels Bohr Institute, Physics of Ice, Climate and Earth, University of Copenhagen, Copenhagen, Denmark, <https://orcid.org/0000-0001-6918-1151> (IF); <https://orcid.org/0000-0001-5292-5249> (KM); 4. Department of Geosciences, Princeton University, Princeton, New Jersey, U.S.A., <https://orcid.org/0000-0002-2742-8299> (JT); 5. Mondaic AG, Impact Hub Zürich, Zurich, Switzerland, <https://orcid.org/0000-0001-6408-6681> (DS)

*Corresponding authors: cecilia.duran@eaps.ethz.ch; amir.khan@eaps.ethz.ch

© Seismological Society of America

In the absence of large events that routinely excite normal modes, the observation of Earth's background-free oscillations or Earth's hum has served as an alternative means of deriving information on the source and structural parameters (e.g., Nishida *et al.*, 2009; Nishida, 2014). Earth's background-free oscillations are primarily fundamental spheroidal and toroidal modes (e.g., Kobayashi and Nishida, 1998; Nawa *et al.*, 1998; Suda *et al.*, 1998; Tanimoto *et al.*, 1998; Ekström, 2001; Kurrle and Widmer-Schmidrig, 2008; Haned *et al.*, 2015), indicative of near-surface sources (Nishida, 2013) that include, as a primary source, ocean infragravity waves (Rhie and Romanowicz, 2004; Webb, 2007), and an acoustic resonance between the atmosphere and the solid Earth (e.g., Tanimoto and Um, 1999; Nishida *et al.*, 2000; Kobayashi, 2008).

Although application of normal-mode seismology to Mars has been considered theoretically and as part of premission science studies (e.g., Okal and Anderson, 1978; Lognonné *et al.*, 1996; Gudkova and Zharkov, 2004; Lognonné and Johnson, 2015; Zheng *et al.*, 2015; Panning *et al.*, 2017; Zharkov *et al.*, 2017; Bissig *et al.*, 2018), the catalog of recorded events, which now numbers in excess of 2700 (Ceylan *et al.*, 2022; Interior Exploration using Seismic Investigations, Geodesy, and Heat Transport [InSight] Marsquake Service, 2023), are all too small to excite normal modes convincingly. Yet, in analogy with excitation of Earth's hum through loading of the solid Earth by atmospheric pressure variations (e.g., Tanimoto and Um, 1999), Mars's atmosphere with its persistently strong winds throughout the day and over the entire duration of the seismic experiment, has also been predicted to excite normal modes or Mars's background-free oscillations (e.g., Kobayashi and Nishida, 1998; Tanimoto, 2001; Lognonné and Johnson, 2015; Lognonné *et al.*, 2016; Nishikawa *et al.*, 2019).

This was considered in detail by Nishikawa *et al.* (2019), who, based on global circulation models of the atmospheric-induced pressure and wind stresses on the solid surface, showed that the latter is potentially strong enough to excite Mars's background-free oscillations so that if enough daily seismic spectra could be stacked to improve the signal-to-noise ratio (SNR), detection of the background-free oscillations could be possible. The crucial unknowns, however, are the levels of background seismic noise, atmospheric forcing, and extent of atmosphere-solid body coupling, which could only be assessed once the instrument was deployed on the surface and its response evaluated (see Pinot *et al.*, 2024, a summary view of the seismic noise evolution during the mission).

Over the course of the mission, the Seismic Experiment for Interior Structure (SEIS) detected many large-amplitude non-seismic disturbances, termed glitches (Scholz *et al.*, 2020) (to be explained in the following), which are found to affect the seismometer response at long periods (10–1000 s), impacting the search for normal modes (Lognonné, Schimmel, *et al.*, 2023). A prerequisite is therefore to remove nonseismic disturbances in the data (henceforth deglitch) prior to normal-mode data processing as will be explained in more detail in what follows.

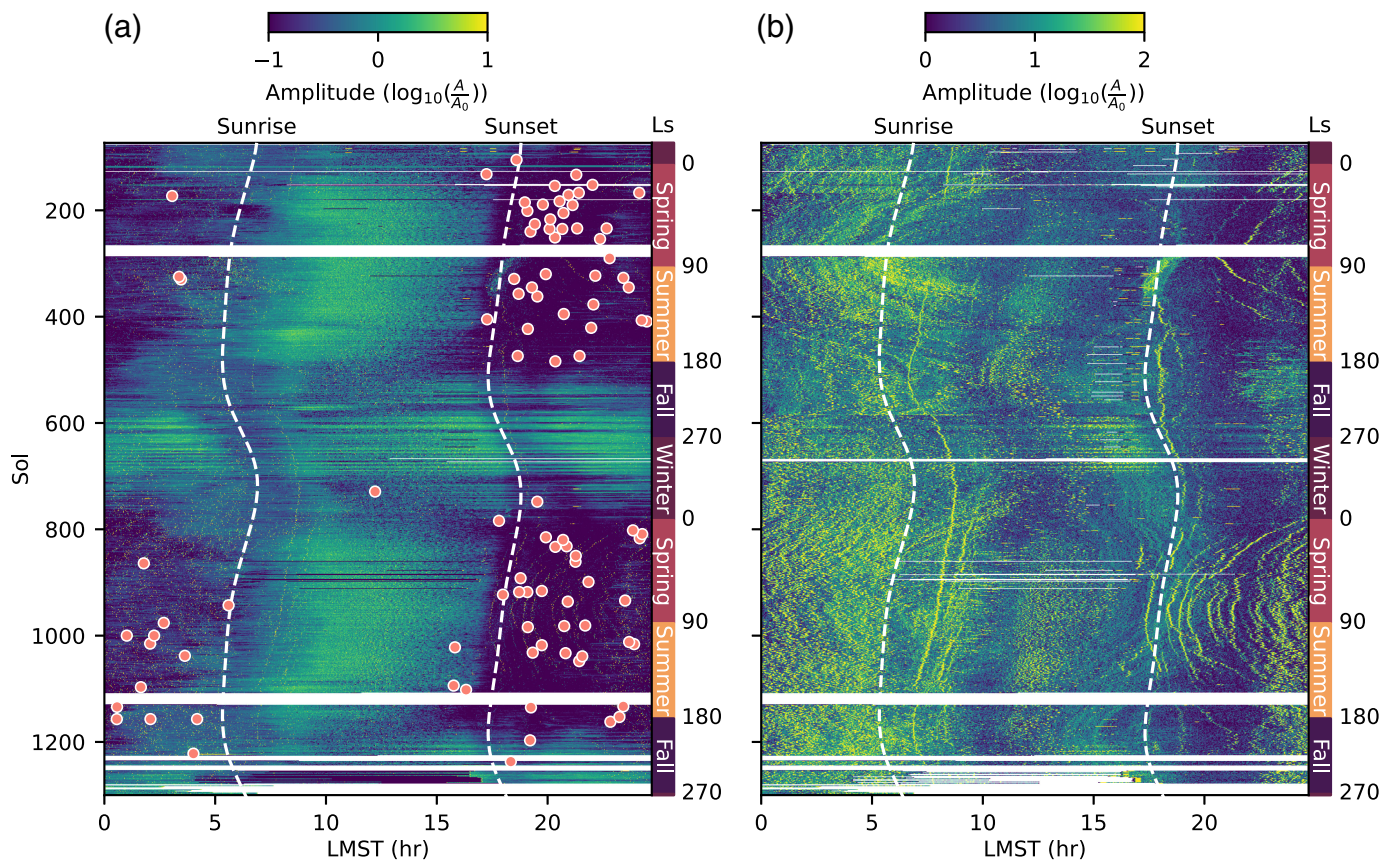
In this study, we provide an analysis of the entire continuous SEIS data set, covering 966 Sols in search of Mars's-free background oscillations. We first provide an overview of the InSight seismic data set, after which waveform deglitching is described. Following this, we compute daily amplitude spectra and stack these to detect normal-mode peaks. To test and verify our processing methods, we apply the same processing scheme to data from terrestrial stations, although we have to note that the nature of the excitation mechanism of the background-free oscillations and the levels of background noise differ between the two planets.

InSight Seismic Data Overview

Despite efforts to mitigate the influence of local weather conditions (wind) and lander noise on SEIS signals (Lognonné *et al.*, 2019), the three-component very broadband (VBB) instrument exhibits, as was also the case for the seismic experiment onboard Viking (Anderson *et al.*, 1977; Nakamura and Anderson, 1979), remarkable sensitivity to Martian weather conditions, resulting in significant diurnal and seasonal variations in recorded noise levels. An overview of this pattern is displayed in Figure 1, which shows the noise evolution of the VBB instrument throughout the mission, based on vertical-component velocity waveform envelopes.

From the noise pattern shown in Figure 1a, noise levels are high between midnight and sunrise and significantly increase during the daytime, but decrease substantially just before sunset and remain relatively low throughout the evening hours. This pattern varies with the seasons, however, and while spring and summer exhibit lower noise levels before and after sunrise and sunset, respectively, autumn and winter show a dramatic increase in background seismic noise throughout the entire day because of the onset of storm season. The persistent high noise levels throughout the day have posed challenges in identifying marsquakes since deployment (Clinton *et al.*, 2021) with most events identified during the quiet evening periods in spring and summer (Ceylan *et al.*, 2022; Knapmeyer *et al.*, 2023), as clearly shown in Figure 1a in case of the low-frequency (LF) events (the same holds true for all types of events). This pattern is associated with weak laminar winds prevailing from early morning until sunrise, followed by stronger, thermally driven turbulent winds persisting throughout the day until near sunset (Banfield *et al.*, 2020). A remarkable consistency in the observed noise pattern is apparent during the two Martian years of seismic monitoring.

In addition to wind and pressure perturbations, persistent glitches have posed severe challenges to data analysis. These impulsive artifacts are manifest in the time domain as one-sided pulses with a duration of ~30 s and span a broad spectrum of amplitudes (Scholz *et al.*, 2020; Ceylan *et al.*, 2021). Although glitches can simultaneously occur on all three VBB sensors, about one-third of them affect only a single component. Glitches have been interpreted as a type of transient instrumental self-noise in

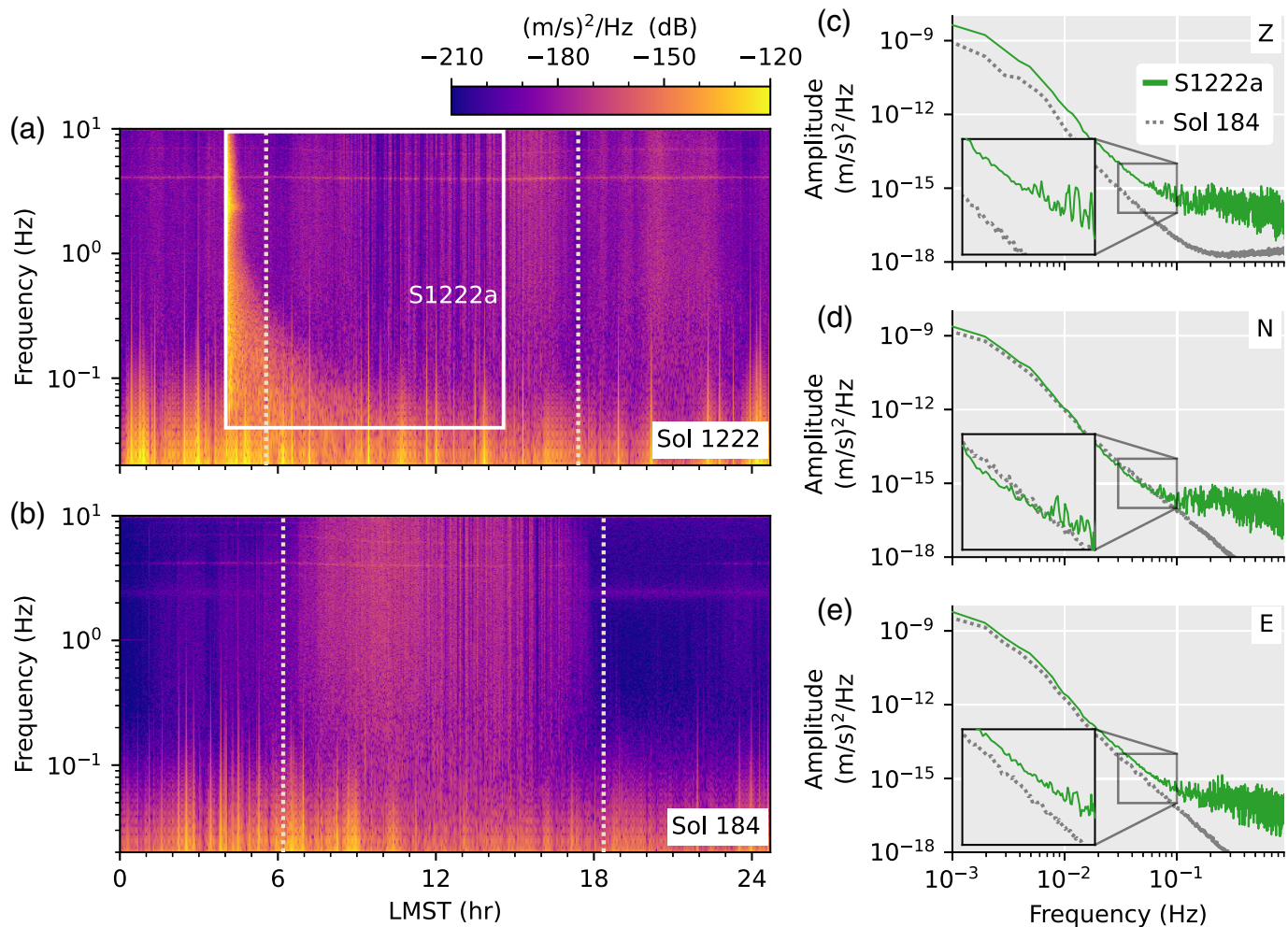


the raw time series controlled by the seismometer's transfer function (Scholz *et al.*, 2020). In Figure 1b, glitches are evident as energy spikes ranging from the lowest frequencies up to almost 1 Hz. Large glitches are most common between midnight and roughly 07:00 LMST (local mean solar time), but they are not easily identifiable once the temperature increases with daybreak. Interestingly, as the mission duration extended into the second Martian year, an apparent increase in the number of glitches became evident. This increase is particularly prominent during daybreak and the early evening, but also present afterward as shown in Figure 1b, in which the glitches are identifiable as high-amplitude signals that repeat throughout the observation period and are especially noticeable during the evening of Spring and Summer of the second Martian year.

Over the lifetime of the mission (February 2019–December 2022), SEIS recorded more than 2700 events (InSight Marsquake Service, 2023). Of these, 98 have been classified by the Marsquake Service as belonging to the family of events labeled the LF events on account of the observation that the main energy is predominantly below 1 Hz. The LF events with moment magnitudes (M_w^{ma} , defined as in Böse *et al.*, 2021) between 2.5 and 4.2 have an overall duration of ~ 10 –30 min and are characterized by relatively clear *P*- and *S*-wave arrivals (Giardini *et al.*, 2020; Clinton *et al.*, 2021; Khan *et al.*, 2021; Ceylan *et al.*, 2022). With predominant propagation through the Martian mantle, these events are similar in character to teleseismic earthquakes (Stähler *et al.*, 2022).

Figure 1. Overview of Martian seismic background noise evolution as recorded by the seismic experiment for interior structure. The images comprise a stack of Sol-long velocity envelopes of vertical-component waveforms that are band-pass filtered between (a) 0.1–1 Hz and (b) 0.01–0.1 Hz. Each amplitude envelope A is normalized by $A_0 = 1$ nm/s. The red circles in panel (a) indicate all recorded 98 low-frequency (LF) events, including marsquakes and meteorite impacts (InSight Marsquake Service, 2023). Interior Exploration using Seismic Investigations, Geodesy, and Heat Transport (InSight) Sols are indicated on the left side of the y-axis, and corresponding solar longitudes (Ls) with Martian seasons (northern hemisphere) are shown on the right side. Time is indicated using local mean solar time (LMST). The figure covers the period from Sol 73, shortly before SEIS started continuous recording, and until the end of the mission (Sol 1439). Sunrise and sunset are indicated by white dashed lines. The white horizontal lines indicate periods of solar conjunction and data gaps. A Sol on Mars is ~ 24 hr 39 min long. The color version of this figure is available only in the electronic edition.

The largest marsquake identified by InSight, which occurred on Sol 1222 (labeled S1222a), has a moment magnitude (M_w^{ma}) of 4.6, surpassing the second-most significant event (S0976a) by a factor of five, and an estimated epicentral distance of $\sim 37^\circ$ (Kawamura *et al.*, 2023). Being the event with the highest SNR recorded by InSight (InSight Marsquake Service, 2023), S1222a has proved valuable in the detection and identification of surface waves, including minor-arc



Rayleigh and Love waves (e.g., [Beghein et al., 2022](#)), and major-arc Rayleigh waves (R2–R7) (e.g., [Kim et al., 2023](#); [Li et al., 2023](#)), and as a possible candidate for the detection of normal modes ([Lognonné, Schimmel, et al., 2023](#)).

A comparison between the vertical-component spectrograms of Sol 1222 and a relatively quiet Sol in the first Martian year (Sol 184) is shown in Figure 2. The event, which is framed by a white box in Figure 2a, is clearly visible in the vertical-component spectrogram, with amplitudes rising markedly above background noise. The occurrence of this event in mid-autumn coincided with a period characterized by elevated noise levels caused by sustained winds ([Ceylan et al., 2022](#)), as evidenced by the background noise depicted in Figure 2a relative to the noise levels visible on Sol 184 (springtime) (Fig. 2b). The energy of S1222a encompasses frequencies ranging from below 0.1 Hz to well above 10 Hz, and it distinguishes itself from other LF events by being part of a subset of events characterized by a very broad frequency range.

Velocity spectra for the event are shown in Figure 2c–e and compared to Sol 184, for which spectra were derived from a 24-hour-long data set. For the computation of velocity spectra, we employed Welch’s (average periodogram) method and segmented the seismic signal into 30-min intervals with a

Figure 2. Analysis of spectral content of event S1222a and sol 184. (a,b) Vertical-component velocity spectrograms of sols 1222 and 184, illustrating the daily background noise recorded by Seismic Experiment for Interior Structure (SEIS). The start and end of event S1222a as determined by the Marsquake Service catalog ([InSight Marsquake Service, 2023](#)) are indicated by vertical lines in panel (a). Sunrise and sunset for each sol are indicated by vertical dotted lines. (c–e) Velocity power spectral density (PSD) was computed for event S1222a and sol 184 across the vertical (Z), North (N), and East (E) components. The color version of this figure is available only in the electronic edition.

50% overlap. The spectral curves exhibit a consistent trend with S1222a evident at frequencies only above 0.05 Hz. Below this, no discernible energy is evident, indicating that the spectra are primarily influenced by environmental and instrumental noise. In addition, synthetic waveform modeling demonstrates that the event’s spectral amplitudes are estimated to be well below the background noise (Fig. S1, in the supplemental material available to this article). This implies that S1222a is not strong enough to have excited LF normal modes as suggested by [Lognonné, Schimmel, et al. \(2023\)](#). We also tried to stack the spectra of several events, including, in addition

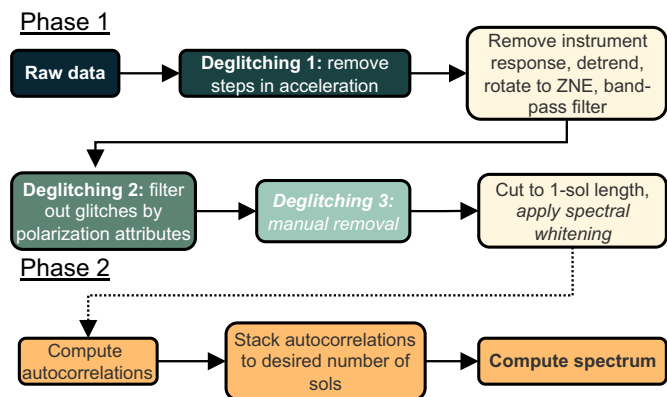


Figure 3. Schematic representation of the data processing workflow. Phase 1 covers the fundamental preprocessing of the seismic data (beige boxes) and deglitching to eliminate non-seismic disturbances (green boxes). Phase 2 covers autocorrelation and stacking (orange boxes). Labels in italics correspond to processing steps that are applied only to the quietest Sols of the mission (Spring–Summer period of the first Martian year). See [Data Processing](#) section for details. The color version of this figure is available only in the electronic edition.

to S1222a, the meteorite impacts S1000a and S1094b (Horleston *et al.*, 2022; Posiolova *et al.*, 2022) but to little avail (Fig. S2). Thus, the only other means of observing normal modes on Mars is through the detection of any atmosphere-induced background-free oscillations as predicted by Nishikawa *et al.* (2019).

Data Processing

The data processing scheme, which involves preprocessing, deglitching, and computation of spectra, is divided into two phases. A schematic illustration of the data workflow is shown in Figure 3, following the methodology outlined by Bensen *et al.* (2007). Phase 1 encompasses data preprocessing (i.e., removal of instrument response, tapering, and filtering) and deglitching, and phase 2 is dedicated to the computation of spectra. Both phases will be detailed in the following.

Phase 1: Data Preprocessing and Deglitching

To compute reliable spectra for stacking, we must first remove any glitches as these contain a wide range of frequencies (Kim *et al.*, 2021) to obtain as clean a data set as possible.

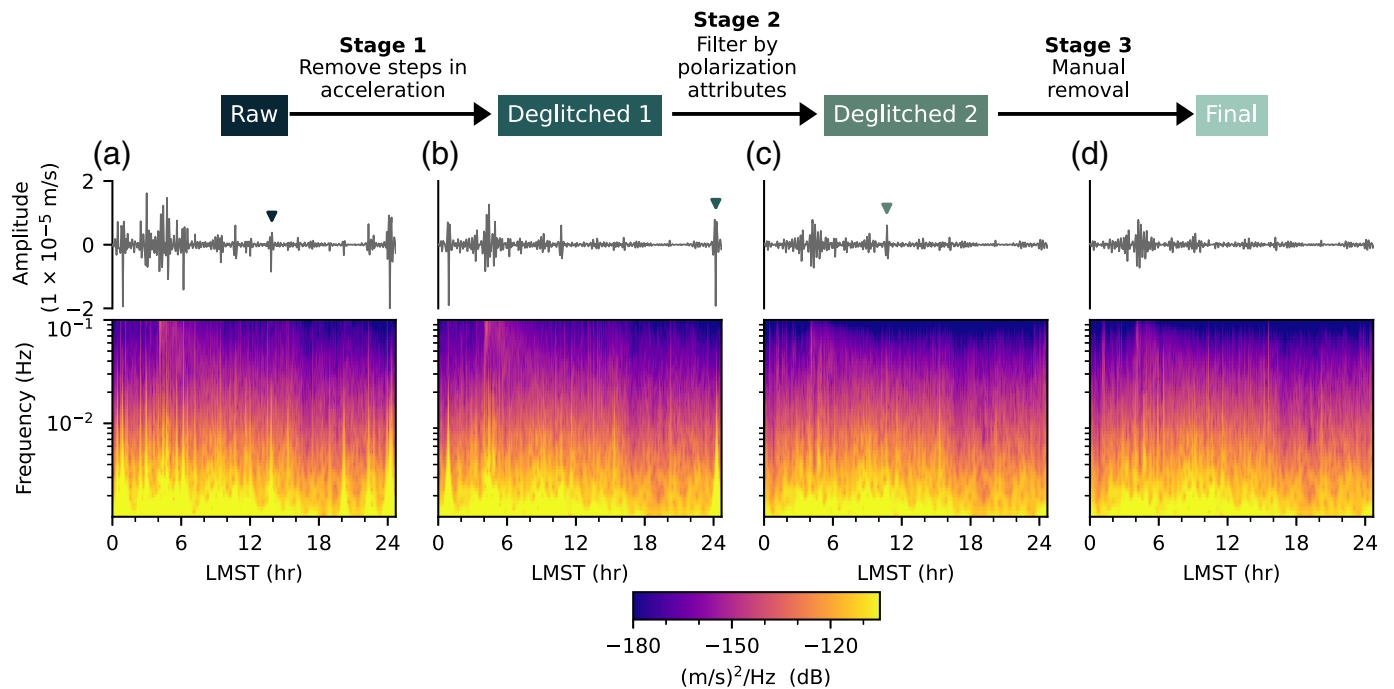
The scheme for deglitching the data is outlined in Figure 4 using Sol 1222 as an example. Given the challenging nature of both identifying (see Barkaoui *et al.*, 2021, for details) and removing glitches using a single algorithm (e.g., Lognonné *et al.*, 2020; Scholz *et al.*, 2020; Xu *et al.*, 2022), our proposed procedure encompasses four stages designed to address this issue. Briefly, the input stage consists of the raw Martian seismograms using the raw VBB components (UVW). Stage 1 corresponds to the deconvolution of the instrument response to

detect and remove glitches through the application of SEISglitch, which was specifically developed for the purpose of handling glitches in the Martian seismic data (Scholz *et al.*, 2020). Subsequently, in stage 2, we filter out most of the remaining glitches by considering the polarization attributes of the signal employing TwistPy (Sollberger, 2023). Finally, any remaining glitches are removed in stage 3 by zero padding these in the time-domain waveforms. Following the removal of glitches from the seismic data, we perform spectral analysis of the deglitched waveforms to hunt for normal modes.

Removal of glitches as acceleration steps

The SEISglitch algorithm of Scholz *et al.* (2020), provides a means of handling glitches in the raw Martian seismic data from the VBB seismometer. Based on the assumption that glitches in the raw data correspond to the convolution of acceleration steps with the seismometer’s instrument response (Lognonné *et al.*, 2020), the algorithm incorporates a sequence of processing steps to effectively detect and eliminate glitches. First, it decimates the three-component seismic data to a lower sampling rate for consistent parameter application and faster computation. Next, the instrument response of each component is deconvolved, transforming the data to acceleration. Subsequently, a band-pass filter is applied to the data to enhance the emergence of acceleration steps. To help identify the glitches more accurately, the algorithm calculates the time derivative of the filtered acceleration data. This emphasizes the impulse-like nature of the acceleration steps, in which a glitch detection is performed using a constant threshold. However, to avoid triggering subsequent samples that exceed the threshold within the same glitch, a window length is introduced, defining the minimum duration of a glitch. This ensures that only individual glitches are captured. Once glitches are successfully detected, they are removed by modeling the raw waveform as a combination of seismometer responses to steps in acceleration and displacement, fitting the model using nonlinear least squares, and then subtracting the fitted glitch from the original data. For further details, readers are referred to Scholz *et al.* (2020).

To search for the optimal parameter configuration for glitch detection, we consider the two parameters that most significantly affect the sensitivity of the detection process. The detection threshold needs to be high enough to avoid triggering on noise while still detecting small glitches. Furthermore, most glitches exhibit a high degree of linear polarization, which can be employed to discriminate against other triggered signals. To analyze the influence of these parameters on the deglitched data, we considered different threshold values ranging from 5×10^{-9} to 5×10^{-11} , and minimum glitch polarization values for the detection between 0.7 and 0.95. The results of this are shown in Figure S3, in which deglitched traces and scalograms are shown for different values of threshold and minimum glitch polarization. Based on this analysis, we conclude that



a threshold value of 5×10^{-10} and a minimum glitch polarization of 0.95 provide the optimal parameter configuration for our study.

We apply SEISglitch to ~ 29 -hr window-long raw seismograms representing the continuous background noise recorded by SEIS. The analysis spans from Sol 73, shortly before SEIS started continuous recording, until the end of the mission (Sol 1439). Each time window initiates 2 hr prior to the considered Sol and extends 2 hr beyond. The deglitched waveforms and three-component scalogram corresponding to the traces for Sol 1222 are shown in Figure 4b (a high-quality version with the three components is shown in Fig. S4).

After removal of glitches from the raw waveforms, data are instrument corrected to velocity, detrended by removing the mean, Hanning tapered (width 0.1), band-pass filtered (0.001–0.1 Hz), and rotated from the UVW components into the geographical reference frame (ZNE).

Following the application of SEISglitch, a substantial portion of high-amplitude glitches have been successfully removed from the data. However, as illustrated in Figure 4b for Sol 1222, a few glitches nevertheless remain in the data. For instance, a significant glitch occurring ~ 1 hr after the beginning of the Sol is evident as a spike in the waveforms. Consequently, we proceed to the next stage of data deglitching.

Removal of glitches employing polarization attributes

To identify nonseismic artifacts like glitches in single-station seismic data analysis, we rely on three-component polarization processing, which provides information about particle motion. Polarization analysis enables the distinction between linearly polarized body waves, elliptically polarized surface waves

Figure 4. Deglitching scheme. The procedure is divided into three stages and includes the raw data input stage in panel (a), followed by three steps of glitch removal: (b) removal of glitches through the application of SEISglitch (Scholz *et al.*, 2020), followed by (c) a filter based on polarization attributes using TwistPy (Sollberger, 2023), and finally by (d) manual removal of glitches. The procedure is illustrated here with the vertical-component velocity waveforms (top) and scalograms (bottom) of sol 1222. Arrows in each panel of the waveforms indicate a glitch that is removed in each subsequent deglitching step. Traces are band-pass filtered between 0.001 and 0.1 Hz. High-quality versions of these panels for all three components are shown in Figures S4–S6. The color version of this figure is available only in the electronic edition.

(Montalbetti and Kanasewich, 1970), and microseismic background noise that generally lacks clear polarization with little preferred directionality (e.g., Haubrich *et al.*, 1963; Tanimoto *et al.*, 2006). The analysis of the polarization attributes of the SEIS data has proved critical in various applications throughout the InSight mission, including the detection of core-reflected *S*-wave phases (Stähler *et al.*, 2021; Durán, Khan, Ceylan, Charalambous, *et al.*, 2022) and in locating marsquakes with a single station (Zenhäusern *et al.*, 2022).

A novel time–frequency domain filtering workflow, Twistpy (Sollberger, 2023), which employs polarization analysis to effectively identify and suppress undesired features in the SEIS data and was introduced by Brinkman *et al.* (2023). TwistPy is capable of detecting and removing glitches, resulting in a larger SNR of the waveforms.

To exploit the advantages of the polarization attributes in the time–frequency domain, TwistPy employs the *S* transform, a special formulation of the continuous wavelet transform that

uniquely combines frequency-dependent time resolution with the localization of real and imaginary spectra (Schimmel and Gallart, 2005). The S transform exhibits a frequency-invariant amplitude response and retains the absolute phase of each localized frequency component, enabling the reconstruction of the time-domain waveforms from the transformed representation. In the time–frequency domain, polarization attributes such as degree of polarization (DOP), ellipticity, azimuth, and inclination are estimated at each point in time and frequency from the eigendecomposition of the complex covariance matrix (Samson and Olson, 1980; Greenhalgh *et al.*, 2018). These attributes can be used to design a nonstationary filter that retains (taking a value of 1) or rejects (taking a value of 0) components of the S transform based on the local polarization attributes. Before applying the filter, the S transform is projected into a coordinate system aligned with the eigenvectors of the covariance matrix, ensuring that the polarization properties of the signal are not altered and that any underlying signal is preserved. Finally, the filtered data are transformed back to the time domain using the inverse S transform, yielding filtered seismograms. For detailed information on the algorithm and methodology, readers are referred to Brinkman *et al.* (2023).

Based on the aforementioned approach, we compute the polarization attributes within a sliding window in both time and frequency. This window extends over five periods in time and operates on the output data obtained after removing the steps in acceleration in the previous section. To keep the computational load within reasonable limits, waveforms are down-sampled to 0.2 Hz. Figure 5 shows the three-component waveforms alongside the ellipticity and DOP for Sol 1222. Large glitches that remain after removing steps in acceleration are easily visible in the time-domain waveforms (indicated by orange vertical bars in Fig. 5a), and are characterized by a low degree of ellipticity and high DOP values (indicated by arrows in Fig. 5b,c). To further refine the filtering process, a filter mask is applied to suppress signals with ellipticity values below 0.15 and DOP values exceeding 0.85. This filtering approach is more conservative compared to the method employed by Brinkman *et al.* (2023) and ensures that the amplitudes at longer periods, in case of non-glitch related signals, remain unaffected. This procedure is applied to the continuous waveforms.

Following the application of the time–frequency domain filtering technique based on polarization attributes, the data are transformed back to the time domain. For Sol 1222, the resulting deglitched vertical-component waveform, along with the three-component scalogram, are shown in Figure 4c (a high-quality version with the three components is shown in Fig. S5). Although large glitches have been effectively eliminated from the data, a few minor glitches may still be present.

The continuous data after the removal of glitches (acceleration steps), followed by filtering based on polarization attributes, are presented in Figure 6 (see raw data in Fig. S7). Generally, most glitches have been successfully removed,

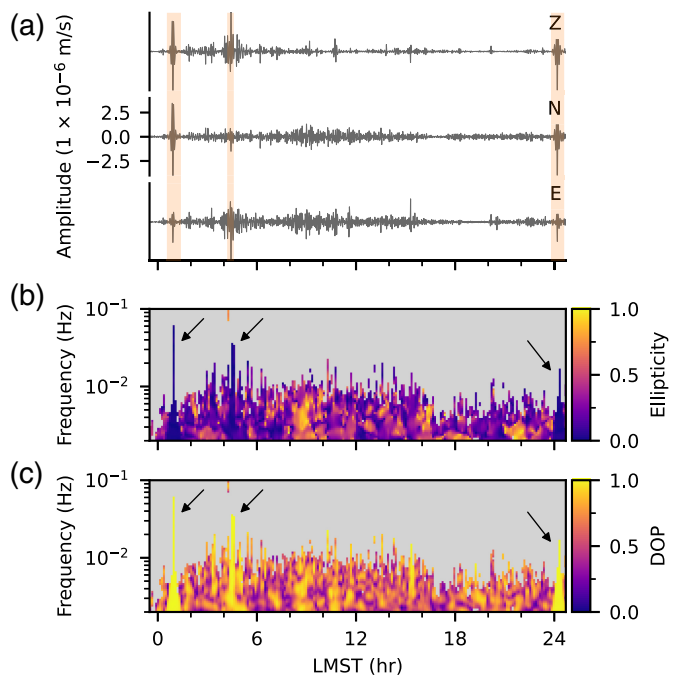
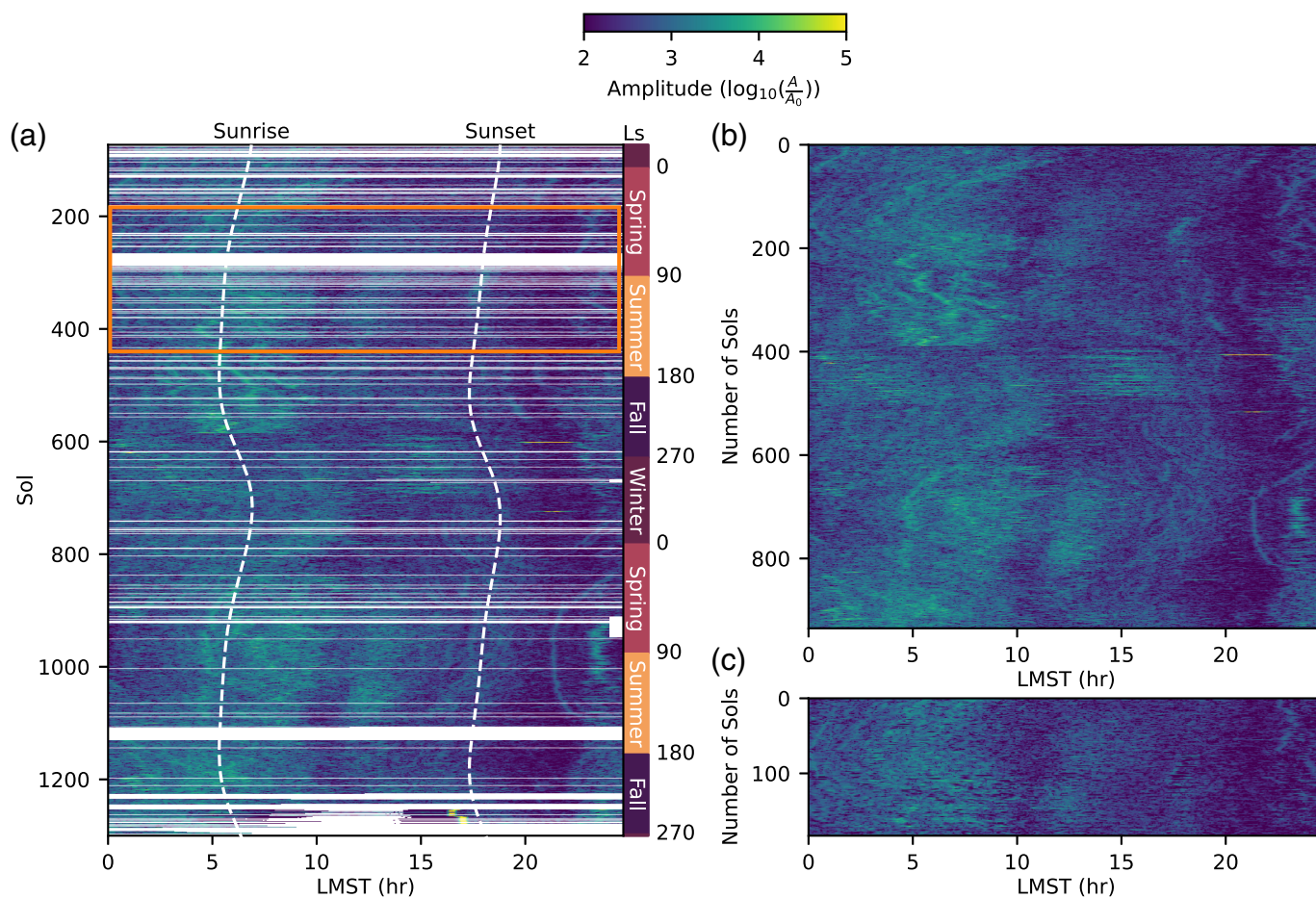


Figure 5. Three-component waveforms and polarization attributes after the first stage of deglitching Sol 1222. Z, N, and E component waveforms are shown in panel (a). Velocity traces are band-pass filtered between 0.001 and 0.1 Hz. The polarization attributes of ellipticity and degree-of-polarization (DOP) are shown as a function of time and frequency for pixels where the signal exceeds two percent of the maximum amplitude measured in the considered time window in panels (b) and (c), respectively. Large glitches are indicated by orange vertical bars in panel (a), low degree of ellipticity (b), and high DOP values (c) (indicated by arrows in panels (b) and (c)). The color version of this figure is available only in the electronic edition.

particularly those associated with daily temperature variations, notably those immediately following sunset and sunrise.

Note that we label the foregoing procedure as “automatic” deglitching. This designation arises from the ability to conduct deglitching operations without the need for manual inspection with the exception of parameter selection. Although this methodology proves effective for the majority of waveforms, instances may arise where large-amplitude glitches remain undetected through algorithm failure (e.g., overlapping glitches in the time–frequency domain, where their superposition destroys linear polarization) or because of contamination by other artifacts (e.g., robot arm activity), requiring the entire Sol to be excluded from the data set (apparent as gaps in Fig. 6a). For visual purposes, a compressed version of Figure 6a without gaps is shown in Figure 6b, which consists of 966 Sols of automatically deglitched data in total. Where minor glitches remain, visual inspection is required. Finally, the entire deglitching procedure reduces spectral amplitudes by a factor of up to 100 (Fig. S2).



Manual removal of glitches

On account of the labor-intensive nature of manually removing glitches, which requires careful inspection of all data components to identify time windows where glitches remain after “automatic” deglitching, we restrict manual inspection to data from Sols 184 to 428, where glitches occur less frequently and data generally exhibit higher SNRs. This corresponds to the spring and summer of the first Martian year (orange rectangle in Fig. 6a). We visually inspect each component using both time series and spectrograms to identify time windows that contain glitches, which are zero-padded.

As an illustration of manual glitch removal, the final vertical-component seismogram and three-component scalogram for Sol 1222 are shown in Figure 4d and shows the manual removal of a glitch at ~11 hr LMST (Fig. 4c). A high-quality version with the three components is shown in Figure S6. Generally, the absence of small-amplitude spikes is noticeable in the final waveform when compared with the “automatically” deglitched waveform (Fig. 4c). An overview of the manually deglitched waveforms (Sols 184–428) is shown in Figure 6c, which consists of a total of 244 Sols of data. In summary, for Mars we thus consider three data sets, comprising (1) set 1: “automatically” deglitched data (Sols 184–428, orange box in Fig. 6a); (2) set 2: manually deglitched data (Sols 184–428, Fig. 6c); and (3) set 3: “automatically” deglitched data from the entire mission (Sols 184–1439, Fig. 6b).

Figure 6. Overview of Martian seismic background noise evolution as recorded by the seismic experiment for interior structure (SEIS) after deglitching. (a–c) Sol-long velocity envelopes of vertical-component band-pass filtered (0.001–0.01 Hz) waveforms. Each amplitude envelope A is normalized by $A_0 = 1$ nm/s. Martian seismic background noise after the removal of glitches employing SEISglitch and polarization attributes is shown in panel (a). InSight Sols are indicated on the left side of the y-axis, and corresponding solar longitudes (Ls) with Martian seasons in the northern hemisphere are shown on the right side. Sunrise and sunset are indicated by white dashed lines. The white horizontal lines indicate solar conjunctions, gaps in the raw data, and all manually removed sols where the deglitching procedure failed (i.e., large glitches were not adequately removed or deglitching algorithms produced an error). A compact version of the panel (a) is shown in (b), in which gaps are omitted for visual purposes. Results after the manual removal of glitches are shown in panel (c), limited to sols spanning from Sol 184 to Sol 427 (orange rectangle in panel a). The color version of this figure is available only in the electronic edition.

Before computing seismic spectra, the deglitched waveforms are trimmed to ~26 hr and 40 min. The beginning and end of each time window are aligned so that it begins 1 hr before the start of each Sol and ends 1 hr following the end of each Sol, respectively. The time windows are of sufficient length to ensure that enough cycles of the longest period

associated with normal modes on Mars (~ 1000 s) are sampled. Given that spectral whitening can enhance the detection of normal modes and mitigate the effects of frequency-localized noise sources, we test it in our analysis by applying it to auto-correlations. This procedure involves spectrally whitening the Fourier-transformed data, where a cosine taper is applied to the low- and high-frequency edges, setting the amplitudes to 1 within the pass band while preserving phase information. The processed data are then transformed back to the time domain. This technique enables a more effective comparison between different methods by flattening the spectra within the targeted frequency range.

Phase 2: Spectral Computation and Analysis

Based on the deglitched data sets, we turn to spectral estimation through cross-correlation, followed by stacking (phase 2). In this study, we focus on vertical-component data because (1) noise levels are generally higher on the horizontal components and (2) the atmosphere-solid body coupling is primarily going to excite (fundamental) spheroidal modes (Nishikawa *et al.*, 2019).

As we work with single-station data, we cross-correlate each trace with itself to obtain the autocorrelation, which is a widely used measure of similarity between a time series, sampled at a discrete set of times t , and a delayed version of itself,

$$CC(\tau) = \sum_{t=1}^T s_1(t)s_2(t + \tau), \quad (1)$$

in which $s_1(t) = s_2(t)$ for the autocorrelation and τ is the time delay. Following Schimmel *et al.* (2018), we employ different cross-correlation approaches to account for the signal characteristics. For this purpose, we employ a geometric normalization to reduce energy sensitivity and render the correlation invariant to amplitude changes between data sets (Schimmel *et al.*, 2018). This geometrically normalized cross-correlation (CCGN) is defined as

$$CCGN(\tau) = \frac{\sum_{t=1}^T s_1(t)s_2(t + \tau)}{\sqrt{\sum_{t=1}^T s_1^2(t)}\sqrt{\sum_{t=1}^T s_2^2(t + \tau)}}. \quad (2)$$

Similarly, the phase cross correlation (PCC) of Schimmel (1999), relies on the instantaneous phases ($\Phi(t)$ and $\Psi(t)$) of the analytic signal for time series $s_1(t)$ and $s_2(t)$, respectively, and is given by

$$PCC(\tau) = \frac{1}{2T} \sum_{t=1}^T |e^{i\Phi(t)} + e^{i\Psi(t+\tau)}|^v - |e^{i\Phi(t)} - e^{i\Psi(t+\tau)}|^v. \quad (3)$$

The PCC is explicitly amplitude unbiased, relying solely on the instantaneous phases derived from the theory of analytic signals. These instantaneous phases contain information from neighboring samples that characterize the waveform as a

function of time. By evaluating waveform similarity through phase-coherent samples, the PCC distinguishes itself from amplitude product summation. Here, all three approaches (CC, CCGN, and PCC) are employed for improved robustness as demonstrated by Schimmel *et al.* (2018).

To achieve a stable response, the 1-Sol long autocorrelations need to be averaged over extended time periods. Stacking over progressively longer time series not only enhances the SNR (Bensen *et al.*, 2007), but also enhances the azimuthal coverage of the noise wavefield (e.g., Snieder, 2004), which is a condition for seismic interferometry. Various stacking techniques have been employed in seismology. Although the linear stack is commonly employed within the seismological community, it may fail to suppress noise, as noncoherent large-amplitude features can still emerge in the stack. The nonlinear n th-root stacking technique (Muirhead, 1968) has proven effective in detecting weak phases (e.g., Richards and Wicks, 1990; Kawakatsu and Niu, 1994). Analogous to the PCC, the phase-weighted stack (PWS) utilizes the instantaneous phase to weight the samples of a standard linear stack (Schimmel and Paulssen, 1997). For consistency, we apply all three aforementioned stacking techniques: linear stacking, n th-root stacking, and PWS.

Before computing the final spectrum of the data, the stacked autocorrelations are Hanning tapered, and the time series are zero-padded to a length equal to the next power of two samples. We compute the amplitude spectrum, using both a conventional fast Fourier transform and a multitaper (MTS) method. The latter makes use of a series of orthogonal tapers to compute multiple independent estimates of the spectrum, effectively suppressing random variability while maintaining a high-resolution estimate (see Thomson, 1982, for details). Finally, we should note that events have not been filtered out since these are not strong enough, as demonstrated for S1000a, S1094b, and S1222a, to measurably excite normal modes on Mars.

Results Earth

As a means of validating our methodology on data from single stations, we apply our processing scheme to terrestrial seismic data from two stations: the Black Forest Observatory (BFO) and Cocos Island (COCO), which are representative of stations set in very quiet and very noisy (island) environments, respectively. To simulate the limited data availability for Mars, we consider 244 days of data from BFO and COCO, which corresponds to the number of manually deglitched Sols of Martian data (Fig. 6c). Days with earthquakes of magnitude $M_w \geq 5.5$ are excluded from the BFO and COCO data sets. Apart from omitting the deglitching steps required for Martian waveforms, processing follows the scheme outlined in Figure 3.

Individual daily spectra obtained from cross-correlation (equation 1) and the final linear stacked spectrum are shown in Figure 7. The spectral whitening step is skipped because the amplitude spectra are relatively flat in the main frequency

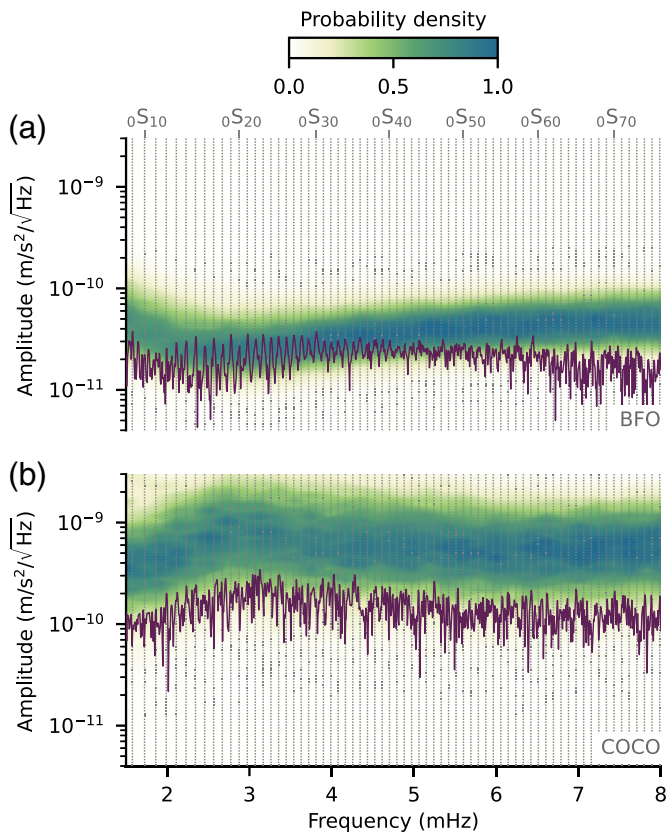


Figure 7. Acceleration power density spectra for stations Black Forest Observatory (BFO) and Cocos Island (COCO) on Earth. Daily amplitude spectra (contoured probability densities) and final linear stack (dark purple line) for (a) BFO and (b) COCO are shown, respectively, and are computed from the square root of the amplitude spectra based on cross-correlation. The daily spectra cover a span of 244 days, excluding those with events of magnitude $M_w \geq 5.5$, and include 24-hr-long autocorrelations. Predictions of fundamental spheroidal modes ($0S_l$) for Preliminary Reference Earth Model (PREM) (Dziewonski and Anderson, 1981), computed using `specnm` (Kemper et al., 2021), are depicted as vertical dotted lines. Note that the final stack shown here is computed by averaging the individual autocorrelations and then calculating the spectrum, rather than stacking the individual spectra. The color version of this figure is available only in the electronic edition.

range of interest (~ 2 – 8 mHz). We observe that while the individual spectra (contoured probability densities) lack clear modal structure and exhibit considerable variability in amplitude, the linear stack (dark purple spectra), particularly for BFO, shows clear spectral peaks in the frequency range of 2–5 mHz that align with the predicted central frequencies of the fundamental spheroidal modes (vertical lines in Fig. 7) for PREM (Dziewonski and Anderson, 1981). These spectral peaks correspond to Earth’s background-free oscillations that are produced by atmosphere- and ocean-solid Earth coupling (e.g., Kobayashi and Nishida, 1998; Nawa et al., 1998; Suda et al., 1998; Webb, 2007; Nishida, 2013). The distinctive

“comb” shape of the stacked spectrum serves as a visual cue of the excitation of Earth’s hum (e.g., Kurrle and Widmer-Schmidrig, 2008). Thus, Figure 7 demonstrates that Earth’s hum can be retrieved from as little as 244 days of single-station data for BFO. In comparison, for a noisy ocean island station such as COCO, with background noise levels an order of magnitude above those of BFO, the “comb” shape of the stacked spectrum is only barely visible in the 2–3 mHz frequency range. These terrestrial tests principally serve as a means of benchmarking the proposed methodology but indicate that in the case of a noisy environment, more daily spectra will need to be stacked to improve the SNR, which for COCO amounts to at least 800 days (Fig. S8). Given the more extreme conditions associated with the surface installation of SEIS on Mars, in combination with even lower atmosphere-induced spectral amplitudes (Nishikawa et al., 2019; Lognonné, Schimmel, et al., 2023), the search for the continuous excitation of Mars’s background-free oscillations clearly represents a formidable challenge.

Mars

Daily spectra and the linearly stacked spectrum for the automatically deglitched waveforms from the entire mission (Fig. 6b) are shown in Figure 8a. The final stack of the Martian data, however, does not show clear peaks nor a “comb-like” structure and plots, as in the case of COCO, toward the bottom of the daily spectra, indicating that the latter are stacking incoherently. Moreover, noise levels are an order of magnitude above those of COCO, further complicating normal-mode detection on Mars.

Stacked spectra for the three data sets (automatically deglitched [244 Sols]; manually deglitched [244 Sols]; and entire waveform data set automatically deglitched), using different cross-correlation methods (PCC and CCGN), in conjunction with MTS for spectral estimation, are shown in Figure 8c. Comparison of final PCC and CCGN stacks for sets 1 and 2 indicates minimal differences in the location of peaks but some variability in amplitudes. The observation that peaks are highly correlated between sets 1 and 2 implies that “automatic” deglitching is permissible and therefore applicable to the entire 966-Sol data set (set 3). For set 3, the consistency between the stacked spectra computed using PCC and CCGN has improved relative to what was observed for sets 1 and 2, noticeably in terms of relative amplitudes. In the frequency range, where normal-mode peaks are expected to stack coherently (2–4 mHz, purple box in Fig. 8c), a high degree of correlation between the location of spectral peaks is visible with both PCC and CCGN showing peaks at, for example, ~ 2 , 3, and 3.8 mHz. Most of these peaks are also visible in the stacks of sets 1 and 2.

To aid in the detection of possible normal-mode peaks, and in line with the identification of fundamental-mode free oscillation peaks in the spectra from BFO and COCO (the eigenfunctions of the first overtone have near-zero surface displacement Fig. S9, implying that overtones are not excited to any appreciable extent by a surface source), we computed central

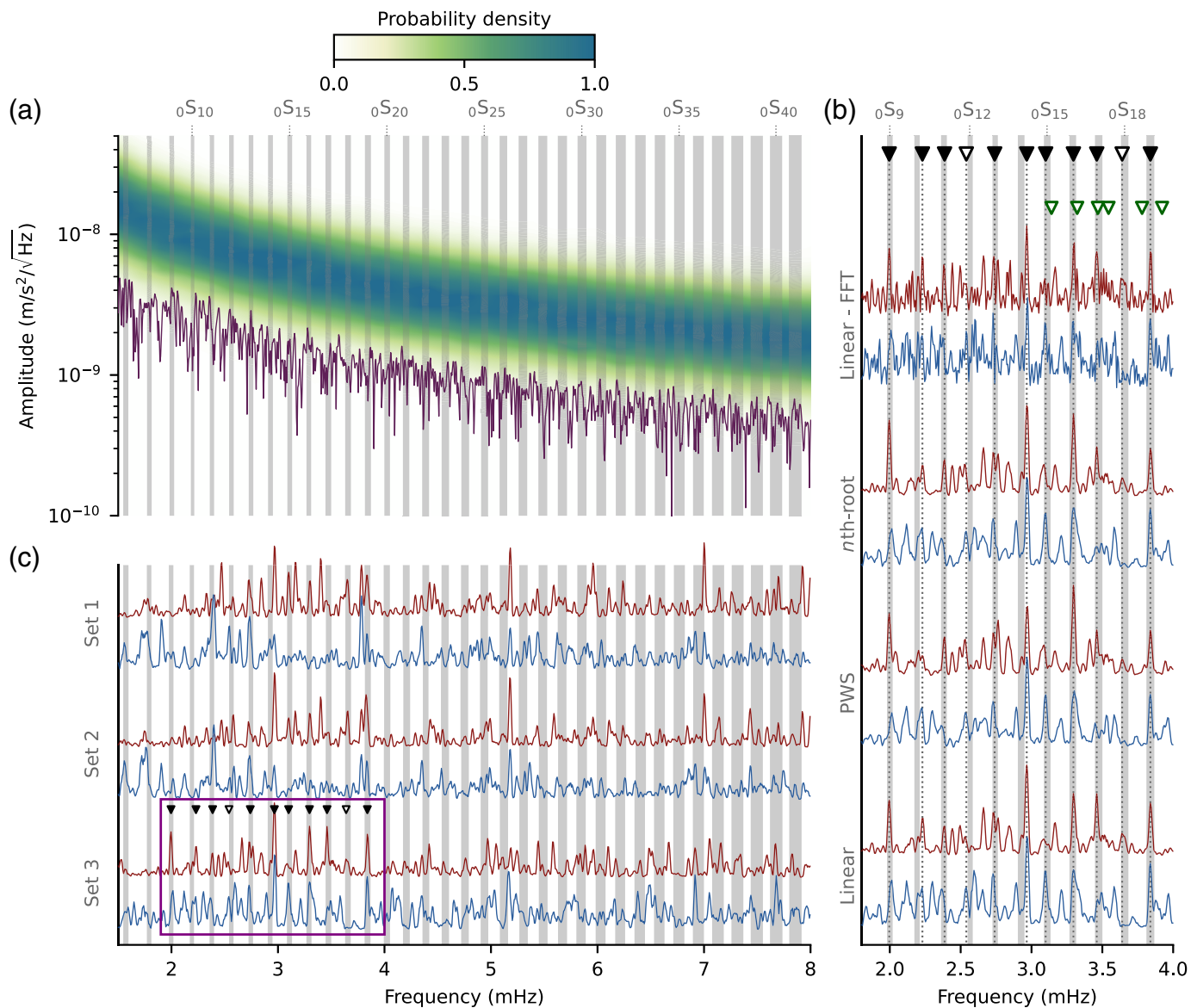


Figure 8. Acceleration power density spectra for Mars. (a) Daily (square root) amplitude spectra (contoured probability densities) and (linear) final stack (dark purple) are computed using the cross-correlation (CC) method. The daily spectra are based on auto-correlations of 966 automatically deglitched 1 Sol-long waveforms. (b) Comparison of the final stack for set 3 using different stacking techniques (indicated on the left side of the spectra) and two techniques for computing spectra MTS (red) and the fast Fourier transform (FFT, blue). The stacking techniques include linear stacking, phase-weighted stacking (PWS) with a power exponent $\nu = 1$, and n th-root stacking with a power exponent $\nu = 1$. The black solid and open triangles indicate peaks that are consistent and less consistent across data sets and stacking techniques, respectively, and open green triangles indicate picks by Lognonné, Schimmel, et al. (2023). Spectral whitening and normalization has

been applied in panels (b) and (c). (c) Comparison of the final stack obtained by employing two cross-correlation methods such as phase cross-correlation (PCC, blue) and geometrically normalized cross-correlation (CCGN, red), in conjunction with multitaper spectral estimation (MTS). Three data sets are investigated: the mission's quietest period, automatically deglitched, covering 244 Sols (set 1); as set 1 including manual deglitching (set 2); the entire mission data, automatically deglitched (set 3). The purple rectangle indicates spectral peaks that are consistent across spectral estimators and stacking techniques and that align with predicted central frequencies (vertical gray bands) computed using *specnm* (Kemper et al., 2021) for a range of Martian seismic models derived from body-wave analysis (Khan et al., 2023). The final stacks for each data set are based on linear stacking. The color version of this figure is available only in the electronic edition.

frequencies for a range of Martian fundamental spheroidal modes (${}_0S_\ell$) in the 2–8 mHz frequency range, which largely illuminate crust and mantle structure (sensitivity kernels are shown

in Fig. S10). For this, we rely on the models of Khan et al. (2023), which were obtained from the inversion of body-wave travel-time data, *P*-to-*s* receiver functions, and mean mass and

normalized moment of inertia. The predicted central frequencies are shown as vertical gray bands in Figure 8, the width of which covers the range of the sampled body-wave models. Note that the vertical bars widen as mode frequency increases, making detection/identification more difficult above 6 mHz. For a peak to be considered as a possible normal mode, the following criteria have to be satisfied: (1) a peak has to be present across the different data sets and spectral estimators; (2) a peak has to be consistent in both frequency and amplitude across the different stacking techniques; and (3) it should preferably align with the predicted central frequencies. These criteria are rather conservative, ensuring that only the most consistent set of peaks are picked.

Despite the observations that peak amplitudes are seen to vary across the stacked spectra for the three data sets, including both PCC and CCGN, as expected given the different levels of deglitching applied to each, it is nevertheless possible to identify a handful of spectral peaks that are in accord with our criteria in the 2–4 mHz frequency range (indicated by inverted triangles). To further test the robustness of these peaks across different stacking methods, we compare linear, phase-weighted, and n th-root stacks (for set 3), which are shown in Figure 8b. The spectral peaks appear to be robust across the different stacking techniques in terms of frequency and for the most part also in amplitude. The consistency of the peaks (in frequency and amplitude) across the different stacking and spectral estimation methods, including the alignment with the predictions, may be considered evidence in support of the identification of these peaks with Mars’s background-free oscillations. The potential fundamental spheroidal normal-mode peaks are summarized in Table 1.

In an attempt to improve the SNR, we used feature extraction and clustering as a means of identifying a subset of the 966 Sol-data set (set 3) that possibly stacks more coherently. After spectral whitening, feature vectors containing the frequencies of the 30 most dominant peaks (60 in the case of BFO), corresponding to the number of predicted fundamental spheroidal modes present in the 2–8 mHz range (indicated by the vertical gray bars in Figs. 7a and 8a), were extracted from each single-Sol and daily spectrum (contoured probability density spectra in Figs. 7a and 8a), respectively. Clustering was subsequently carried out using a distance measure based on a simple L2-norm misfit between feature vectors (see Section S2 for more details). For BFO this resulted in four clusters (Fig. S11a), whereas for Mars only a single cluster is discernable (Fig. S11b), indicating that outliers are not clearly distinguishable in the Martian data set.

To independently corroborate the identified peaks in the stacked spectrum for Mars (Fig. 8), we next searched for possible persistent, that is, recurring, peak frequencies in the daily spectra. For this, we looked for and computed the distribution of frequencies in the 2–8 mHz range (henceforth labeled spectral peak density) in the daily spectra of set 3, that is, for each daily spectrum we counted the number of the most dominant spectral peaks as a function of frequency and plotted their

TABLE 1

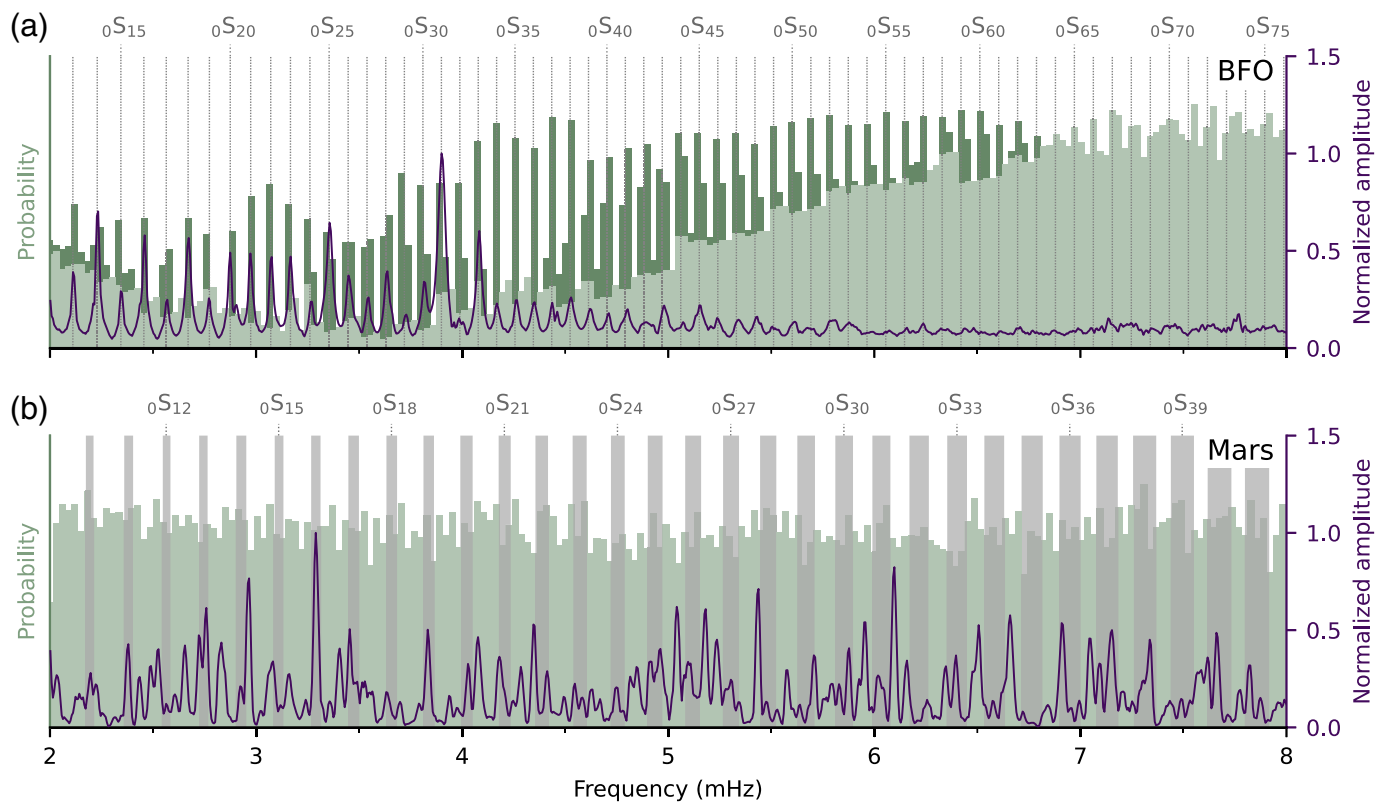
Central Frequency, Period, and Mode Label (${}_0S_\ell$) of Potential Fundamental Spheroidal Normal-Mode Candidates

Central Frequency (mHz)	Period (s)	Mode
1.99	501.05	${}_0S_9$
2.23	447.66	${}_0S_{10}$
2.38	419.04	${}_0S_{11}$
2.74	366.54	${}_0S_{13}$
2.96	337.17	${}_0S_{14}$
3.10	322.58	${}_0S_{15}$
3.29	303.41	${}_0S_{16}$
3.46	288.96	${}_0S_{17}$
3.83	260.47	${}_0S_{19}$

distribution in the form of a histogram. The underlying assumption is that the spectral peak density of random noise will be flat, whereas any recurring, that is, persistent, peaks, are expected to stack coherently and thus result in an informative, that is, nonflat spectral peak density. This represents an independent means of verifying the stacked spectra regardless of whether peaks are small or large.

The resultant spectral peak density is shown in Figure 9 for BFO and the InSight data in the frequency range 2–8 mHz together with the corresponding stacked spectra (dark purple lines) and predicted fundamental-mode central frequencies (vertical gray bars). In the case of BFO—our benchmark—the spectral peak density (dark green bins in Fig. 9a) is, as expected, strongly correlated with the peaks in the stacked spectrum and the location of the predicted fundamental-mode spheroidal frequencies computed using PREM. Where the stacked spectrum shows clearly identifiable peaks to ~5.5 mHz, the spectral peak density can extend this range to ~6.5 mHz, beyond which the normal-mode peaks become buried in environmental noise (light green bins in Fig. 9). The latter decreases from 2 mHz, reaching a minimum between 3 and 4 mHz, after which it slowly increases and reaches a maximum beyond 7 mHz. In the case of the Martian data, however, the clear pattern of BFO is absent. We see no peaks in the spectral peak density that rise clearly above the background environmental noise, and no correlation with neither the stacked spectrum nor the predictions based on the body-wave models, as in the case of BFO. This suggests that normal modes associated with Mars’s background-free oscillations, while undoubtedly excited by the atmosphere as suggested by Nishikawa *et al.* (2019), are not independently verifiable with the current data set (see also Figs. S11–S12).

In view of the slightly more than four years of near-continuous seismic recording on Mars, we are now able to make quantitative estimates of the moment magnitude required to observe



normal modes. Figure S13 indicates that to observe normal modes above 3 mHz with InSight, a moment magnitude over 6 ($>1 \cdot 10^{18}$ N · m) is required, which is only slightly higher than previous estimates that relied on a premission noise model (e.g., Bissig *et al.*, 2018; Nishikawa *et al.*, 2019). Based on theoretical estimates and waveform simulations, Nishikawa *et al.* (2019) argued that the atmosphere-excited background-free oscillations on Mars on a Sol-by-Sol basis would be similar to a magnitude-5 ($5 \cdot 10^6$ N · m) event, which, as shown in Figure S13, lies several orders of magnitude below the observed noise floor. It was further argued that by stacking a full year of Martian seismic data, an order-of-magnitude improvement in spectral amplitudes could be achieved. Yet, Figure S13 shows that as a minimum a three order-of-magnitude increase in amplitudes is required to level with the noise floor. This observation may also explain the noninformative nature of the spectral peak density associated with the Martian seismic data that we currently observe (Fig. 9b).

Finally, Lognonné, Schimmel, *et al.* (2023) have reported the detection of (1) normal modes based on the largest observed marsquake S1222a and (2) the background-free oscillations of Mars relying on a single Sol of noise preceding S1222a. Figure 2c–e and Figure S1, however, demonstrated that S1222a is of insufficient magnitude to have excited normal modes on Mars. Moreover, the preceding analysis has shown that Mars’s background-free oscillations are not extractable from a single Sol of noise. On account of the evidence presented herein, the “detected” peaks of Lognonné, Schimmel, *et al.* (2023) may therefore be a product of their analysis method.

Figure 9. Comparison of stacked spectra, normal-mode predictions, and spectral features (peaks) based on clustering analysis. Stacked spectra (purple) for (a) seismic data recorded at BFO and (b) Mars InSight data (set 3), shown together with their respective spectral peak densities (light and dark green histograms) and the fundamental spheroidal mode central frequencies (gray vertical bars) predicted using PREM and the Martian seismic body-wave models of Khan *et al.* (2023). The histograms represent the relative number (probability) of spectral peaks as a function of frequency for (a) all 244 daily spectra recorded at BFO (Fig. 7a) and (b) all 966 Sol spectra (Fig. 8a). The dark green bins correspond to background-free oscillation spectral peaks, whereas light green bins indicate environmental noise. The spectral peak densities represent the probability distributions of the location of the 60 (BFO) and 30 (Mars) most dominant peaks in the frequency range 2–8 mHz. Amplitudes of stacked spectra and spectral peak densities are normalized and scaled for better visualization. The color version of this figure is available only in the electronic edition.

Summary and Conclusions

In this study, we have described a methodology for processing and analyzing the continuous seismic data collected by the Mars InSight mission. In the first phase, we implemented an automated processing scheme aimed at mitigating the impact of the ubiquitous glitches on the InSight seismic data. These artifacts significantly affect amplitude spectra, and reducing their effect is indispensable for detecting normal modes. Both automated and manual deglitching were tested. In a second

phase, we looked for normal modes excited by some of the largest events that were recorded by InSight but found the associated spectral amplitudes to be well below the background noise. In a third phase, we computed spectra from 1-Sol long autocorrelations for the entire data set, consisting of 966 Sols of continuous data, and stacked these to enhance any background-free oscillations present in the data. As a means of verifying our processing and analysis scheme, we applied it to seismic data from Earth.

In agreement with observations of the hum on Earth, we find fundamental spheroidal normal-mode peaks in the spectra that align with predictions based on seismic body-wave models and are consistent across the different data sets and processing and stacking methods investigated, which suggests that some of the peaks may be atmosphere-induced background-free oscillations. Yet, unambiguous detection remains difficult.

A confluence of factors is likely to contribute, including the limited number of Sols of data with useful, that is, coherent, signal, generally extremely high noise levels that are an order of magnitude higher than those of a very noisy terrestrial island station, and, not least, the presence of glitches that, despite careful data treatment, affect the seismic data from the shortest (body waves) to the longest (normal mode) periods. In this connection, manual deglitching of a smaller subset of the continuous data (244 sols) also proved insufficient. This highlights the need for additional deglitching strategies that may improve upon the current impasse, although this is not guaranteed given the available quantity of data. Future missions aiming to study the interior structure of planetary objects using LF seismic signals need to address the issue of suppressing glitches and other noise artefacts more directly through improved temperature stability of the instrumentation.

In summary, we may conclude, in the vain of the lessons learned from the Viking seismic experiment, with a recommendation from the InSight mission: for seismology on Mars to maximize gain, the seismometer should not only be placed on the ground but needs to be removed from full-scale environmental exposure through proper shielding, preferably burial, and possibly on bedrock. This would extend the period where seismic events are detected from $\sim 1/3$ to the entire Sol, hence improving the chances of detecting background-free oscillations, in addition to estimates of seismicity.

Data and Resources

The Interior Exploration using Seismic Investigations, Geodesy, and Heat Transport (InSight) event catalog V14 (comprising all events until the end of the mission) and waveform data are available from the Incorporated Research Institutions for Seismology Data Management Center (IRIS-DMC), National Aeronautics and Space Administration (NASA)-Planetary Data System (PDS), Seismic Experiment for Interior Structure (SEIS)-InSight data portal and Institut du Physique du Globe de Paris (IPGP) data center ([InSight Mars Seismic Experiment for Interior Structure \[SEIS\] Data Service, 2019a](#); [InSight Mars SEIS](#)

[Data Service, 2019b](#); [InSight Marsquake Service, 2023](#)). Seismic waveforms are also available from NASA PDS ([InSight Mars SEIS Data Service, 2019a](#)). The data were processed with ObsPy ([Beyreuther et al., 2010](#)), NumPy ([Harris et al., 2020](#)), SciPy ([Virtanen et al., 2020](#)), SEISGlitch ([Scholz et al., 2020](#)), TwistPy ([Sollberger, 2023](#)), specnm ([Kemper et al., 2021](#)), multitaper ([Prieto, 2022](#)), and visualizations were created with Matplotlib ([Hunter, 2007](#)). Interior Martian structure models from [Khan et al. \(2023\)](#) are available in digital format from doi: [10.18715/IPGP.2023.lxn7e6d](#). Automatically deglitched seismic traces are provided in doi: [10.5281/zenodo.13789563](#). Additional figures and analysis are included in the supplemental material.

Declaration of Competing Interests

The authors acknowledge that there are no conflicts of interest recorded.

Acknowledgments

The authors acknowledge National Aeronautics and Space Administration (NASA), The National Centre for Space Studies of France (CNES), partner agencies, and institutions (UK Space Agency [UKSA], Swiss Space Office [SSO], German Aerospace Center [Deutsches Zentrum für Luft- und Raumfahrt, DLR], Jet Propulsion Laboratory [JPL], Institut du Physique du Globe de Paris [IPGP]-Centre National de la Recherche Scientifique-École Normale Supérieure [CNRS], Eldgenössische Technische Hochschule Zürich [ETHZ], Imperial College London [ICL], Max Planck Institute for Solar System Research [MPS-MPG]), and the operators of JPL, SEIS on Mars Operation Center (SISMOC), Mars SEIS Package Data Service (MSDS), Incorporated Research Institutions for Seismology Data Management Center (IRIS-DMC), and Planetary Data System (PDS) for providing Standard for Exchange of Earthquake Data (SEED) Seismic Experiment for Interior Structure (SEIS) data. C. D., A. K., and D. G. would like to acknowledge support from Eldgenössische Technische Hochschule (ETH) through the ETH+ funding scheme (ETH+02 19-1: “Planet Mars”). I. F. acknowledges support from the Independent Research Fund Denmark (Project “Planetary Vision”, Grant Number 3103-00199B). K. M. would like to acknowledge support from the Inge Lehmann Grant of 1983 for a research visit to ETH. Finally, we are grateful to Göran Ekström and an anonymous reviewer for constructive comments that helped improve the article and to Paul Davis for comments that helped clarify parts of an earlier version of the article. This is InSight contribution 344.

References

- Anderson, D. L., W. F. Miller, G. V. Latham, Y. Nakamura, M. N. Toksöz, A. M. Dainty, F. K. Duennebie, A. R. Lazarewicz, R. L. Kovach, and T. C. D. Knight (1977). Seismology on Mars, *J. Geophys. Res.* **82**, no. 28, 4524–4546.
- Banerdt, W. B., S. E. Smrekar, D. Banfield, D. Giardini, M. Golombek, C. L. Johnson, P. Lognonné, A. Spiga, T. Spohn, C. Perrin, et al. (2020). Initial results from the InSight mission on Mars, *Nature Geosci.* **13**, no. 3, 183–189.
- Banfield, D., A. Spiga, C. Newman, F. Forget, M. Lemmon, R. Lorenz, N. Murdoch, D. Viudez-Moreiras, J. Pla-Garcia, R. F. Garcia, et al. (2020). The atmosphere of Mars as observed by InSight, *Nature Geosci.* **13**, no. 3, 190–198.

- Barkaoui, S., P. Lognonné, T. Kawamura, É. Stutzmann, L. Seydoux, M. V. de Hoop, R. Balestrieri, J. Scholz, G. Sainton, *et al.* (2021). Anatomy of continuous Mars SEIS and pressure data from unsupervised learning, *Bull. Seismol. Soc. Am.* **111**, no. 6, 2964–2981.
- Beghein, C., J. Li, E. Weidner, R. Maguire, J. Wookey, V. Lekić, P. Lognonné, and W. Banerdt (2022). Crustal anisotropy in the Martian Lowlands from surface waves, *Geophys. Res. Lett.* **49**, no. 24, e2022GL101508, doi: [10.1029/2022GL101508](https://doi.org/10.1029/2022GL101508).
- Bensen, G. D., M. H. Ritzwoller, M. P. Barmin, A. L. Levshin, F. Lin, M. P. Moschetti, N. M. Shapiro, and Y. Yang (2007). Processing seismic ambient noise data to obtain reliable broad-band surface wave dispersion measurements, *Geophys. J. Int.* **169**, 1239–1260.
- Beyreuther, M., R. Barsch, L. Krischer, T. Megies, Y. Behr, and J. Wassermann (2010). ObsPy: A Python toolbox for seismology, *Seismol. Res. Lett.* **81**, no. 3, 530–533.
- Bissig, F., A. Khan, M. van Driel, S. C. Stähler, D. Giardini, M. Panning, M. Drilleau, P. Lognonné, T. V. Gudkova, V. N. Zharkov, *et al.* (2018). On the detectability and use of normal modes for determining interior structure of Mars, *Space Sci. Rev.* **214**, no. 8, 114, doi: [10.1007/s11214-018-0547-9](https://doi.org/10.1007/s11214-018-0547-9).
- Böse, M., S. C. Stähler, N. Deichmann, D. Giardini, J. Clinton, P. Lognonné, S. Ceylan, M. van Driel, C. Charalambous, N. Dahmen, *et al.* (2021). Magnitude scales for marsquakes calibrated from InSight data, *Bull. Seismol. Soc. Am.* **111**, no. 6, 3003–3015.
- Brinkman, N., D. Sollberger, C. Schmelzbach, S. C. Stähler, and J. Robertsson (2023). Applications of time-frequency domain polarization filtering to insight seismic data, *Earth Space Sci.* **10**, no. 11, e2023EA003169, doi: [10.1029/2023EA003169](https://doi.org/10.1029/2023EA003169).
- Ceylan, S., J. F. Clinton, D. Giardini, M. Böse, C. Charalambous, M. van Driel, A. Horleston, T. Kawamura, A. Khan, G. Orhand-Mainsant, *et al.* (2021). Companion guide to the marsquake catalog from InSight, Sols 0–478: Data content and non-seismic events, *Phys. Earth Planet. In.* **310**, 106597.
- Ceylan, S., J. F. Clinton, D. Giardini, S. C. Stähler, A. Horleston, T. Kawamura, M. Böse, C. Charalambous, N. L. Dahmen, M. van Driel, *et al.* (2022). The marsquake catalogue from InSight, sols 0–1011, *Phys. Earth Planet. In.* **333**, 106943, doi: [10.1016/j.pepi.2022.106943](https://doi.org/10.1016/j.pepi.2022.106943).
- Clinton, J. F., S. Ceylan, M. van Driel, D. Giardini, S. C. Stähler, M. Böse, C. Charalambous, N. L. Dahmen, A. Horleston, T. Kawamura, *et al.* (2021). The Marsquake catalogue from InSight, sols 0–478, *Phys. Earth Planet. In.* **310**, 106595, doi: [10.1016/j.pepi.2020.106595](https://doi.org/10.1016/j.pepi.2020.106595).
- Drilleau, M., H. Samuel, R. F. Garcia, A. Rivoldini, C. Perrin, C. Michaut, M. Wiczorek, B. Tauzin, J. A. D. Connolly, P. Meyer, *et al.* (2022). Marsquake locations and 1D seismic models for mars from insight data, *J. Geophys. Res.* **127**, no. 9, e2021JE007067, doi: [10.1029/2021JE007067](https://doi.org/10.1029/2021JE007067).
- Durán, C., A. Khan, S. Ceylan, C. Charalambous, D. Kim, M. Drilleau, H. Samuel, and D. Giardini (2022). Observation of a core-diffracted *P*-wave from a farside impact with implications for the lower-mantle structure of mars, *Geophys. Res. Lett.* **49**, no. 21, e2022GL100887, doi: [10.1029/2022GL100887](https://doi.org/10.1029/2022GL100887).
- Durán, C., A. Khan, S. Ceylan, G. Zenhäusern, S. Stähler, J. Clinton, and D. Giardini (2022). Seismology on Mars: An analysis of direct, reflected, and converted seismic body waves with implications for interior structure, *Phys. Earth Planet. In.* **325**, 106851, doi: [10.1016/j.pepi.2022.106851](https://doi.org/10.1016/j.pepi.2022.106851).
- Dziewonski, A. M., and D. L. Anderson (1981). Preliminary reference Earth model, *Phys. Earth Planet. In.* **25**, 297–356.
- Ekström, G. (2001). Time domain analysis of earth's long-period background seismic radiation, *J. Geophys. Res.* **106**, no. B11, 26,483–26,493.
- Giardini, D., P. Lognonné, W. B. Banerdt, W. T. Pike, U. Christensen, S. Ceylan, J. F. Clinton, M. van Driel, S. Stähler, M. Böse, *et al.* (2020). The seismicity of mars, *Nature Geosci.* **13**, 205–212.
- Greenhalgh, S., D. Sollberger, C. Schmelzbach, and M. Ruttly (2018). Chapter two—single-station polarization analysis applied to seismic wavefields: A tutorial, in *Advances in Geophysics*, C. Schmelzbach (Editor), Vol. 59, Elsevier, Amsterdam, The Netherlands, 123–170.
- Gudkova, T., and V. Zharkov (2004). Mars: Interior structure and excitation of free oscillations, *Phys. Earth Planet. In.* **142**, no. 1, 1–22.
- Haned, A., E. Stutzmann, M. Schimmel, S. Kiselev, A. Davaille, and A. Yelles-Chaouche (2015). Global tomography using seismic hum, *Geophys. J. Int.* **204**, no. 2, 1222–1236.
- Harris, C. R., K. J. Millman, S. J. van der Walt, R. Gommers, P. Virtanen, D. Cournapeau, E. Wieser, J. Taylor, S. Berg, N. J. Smith, *et al.* (2020). Array programming with NumPy, *Nature* **585**, no. 7825, 357–362.
- Haubrich, R., W. Munk, and F. Snodgrass (1963). Comparative spectra of microseisms and swell, *Bull. Seismol. Soc. Am.* **53**, no. 1, 27–37.
- Horleston, A. C., J. F. Clinton, S. Ceylan, D. Giardini, C. Charalambous, J. C. E. Irving, P. Lognonné, S. C. Stähler, G. Zenhäusern, N. L. Dahmen, *et al.* (2022). The far side of mars: Two distant marsquakes detected by InSight, *Seism. Rec.* **2**, no. 2, 88–99.
- Huang, Q., N. C. Schmerr, S. D. King, D. Kim, A. Rivoldini, A.-C. Plesa, H. Samuel, R. R. Maguire, F. Karakostas, V. Lekić, *et al.* (2022). Seismic detection of a deep mantle discontinuity within Mars by InSight, *Proc. Natl. Acad. Sci. Unit. States Am.* **119**, no. 42, e2204474119, doi: [10.1073/pnas.2204474119](https://doi.org/10.1073/pnas.2204474119).
- Hunter, J. D. (2007). Matplotlib: A 2d graphics environment, *Comput. Sci. Eng.* **9**, no. 3, 90–95.
- InSight Mars SEIS Data Service (2019a). InSight SEIS data bundle, *PDS Geosciences (GEO) Node* doi: [10.17189/1517570](https://doi.org/10.17189/1517570).
- InSight Mars SEIS Data Service (2019b). SEIS raw data, insight mission, *IPGP, JPL, CNES, ETHZ, ICL, MPS, ISAE-Supaero, LPG, MFSC* doi: [10.18715/SEIS.INSIGHT.XB_2016](https://doi.org/10.18715/SEIS.INSIGHT.XB_2016).
- InSight Marsquake Service (2023). Mars seismic catalogue, insight mission; v14 2023-04-01.
- Irving, J. C. E., V. Lekić, C. Durán, M. Drilleau, D. Kim, A. Rivoldini, A. Khan, H. Samuel, D. Antonangeli, W. B. Banerdt, *et al.* (2023). First observations of core-transiting seismic phases on Mars, *Proc. Natl. Acad. Sci. Unit. States Am.* **120**, no. 18, e2217090120, doi: [10.1073/pnas.2217090120](https://doi.org/10.1073/pnas.2217090120).
- Kawakatsu, H., and F. Niu (1994). Seismic evidence for a 920-km discontinuity in the mantle, *Nature* **371**, no. 6495, 301–305.
- Kawamura, T., J. F. Clinton, G. Zenhäusern, S. Ceylan, A. C. Horleston, N. L. Dahmen, C. Duran, D. Kim, M. Plasman, S. C. Stähler, *et al.* (2023). S1222a—The largest marsquake detected by insight, *Geophys. Res. Lett.* **50**, no. 5, e2022GL101543, doi: [10.1029/2022GL101543](https://doi.org/10.1029/2022GL101543).
- Kemper, J., M. van Driel, F. Munch, A. Khan, and D. Giardini (2021). A spectral element approach to computing normal modes, *Geophys. J. Int.* **229**, no. 2, 915–932.

- Khan, A., S. Ceylan, M. van Driel, D. Giardini, P. Lognonné, H. Samuel, N. C. Schmerr, S. C. Stähler, A. C. Duran, Q. Huang, *et al.* (2021). Upper mantle structure of Mars from InSight seismic data, *Science* **373**, no. 6553, 434–438.
- Khan, A., D. Huang, C. Durán, P. A. Sossi, D. Giardini, and M. Murakami (2023). Evidence for a liquid silicate layer atop the Martian core, *Nature* **622**, no. 7984, 718–723.
- Khan, A., P. Sossi, C. Liebske, A. Rivoldini, and D. Giardini (2022). Geophysical and cosmochemical evidence for a volatile-rich Mars, *Earth Planet. Sci. Lett.* **578**, 117330, doi: [10.1016/j.epsl.2021.117330](https://doi.org/10.1016/j.epsl.2021.117330).
- Kim, D., W. B. Banerdt, S. Ceylan, D. Giardini, V. Lekić, P. Lognonné, C. Beghein, É. Beucler, S. Carrasco, C. Charalambous, *et al.* (2022). Surface waves and crustal structure on Mars, *Science* **378**, no. 6618, 417–421.
- Kim, D., P. Davis, V. Lekić, R. Maguire, N. Compaire, M. Schimmel, E. Stutzmann, J. C. E. Irving, P. Lognonné, J. Scholz, *et al.* (2021). Potential pitfalls in the analysis and structural interpretation of seismic data from the Mars insight mission, *Bull. Seismol. Soc. Am.* **111**, no. 6, 2982–3002.
- Kim, D., C. Durán, D. Giardini, A.-C. Plesa, S. C. Stähler, C. Boehm, V. Lekić, S. M. McLennan, S. Ceylan, J. F. Clinton, *et al.* (2023). Global crustal thickness revealed by surface waves orbiting Mars, *Geophys. Res. Lett.* **50**, no. 12, e2023GL103482, doi: [10.1029/2023GL103482](https://doi.org/10.1029/2023GL103482).
- Knapmeyer, M., S. Stähler, A.-C. Plesa, S. Ceylan, C. Charalambous, J. Clinton, N. Dahmen, C. Durán, A. Horleston, T. Kawamura, *et al.* (2023). The global seismic moment rate of Mars after event S1222a, *Geophys. Res. Lett.* **50**, no. 7, e2022GL102296, doi: [10.1029/2022GL102296](https://doi.org/10.1029/2022GL102296).
- Knapmeyer-Endrun, B., M. P. Panning, F. Bissig, R. Joshi, A. Khan, D. Kim, V. Lekić, B. Tauzin, S. Tharimena, M. Plasman, *et al.* (2021). Thickness and structure of the Martian crust from InSight seismic data, *Science* **373**, no. 6553, 438–443.
- Kobayashi, N. (2008). Infrasonds and background free oscillations, *8th International Conference on Theoretical and Computational Acoustics (ICTCA 2007)*, Heraklion, Greece, 2–6 July 2007, 105–114.
- Kobayashi, N., and K. Nishida (1998). Continuous excitation of planetary free oscillations by atmospheric disturbances, *Nature* **395**, no. 6700, 357–360.
- Kurrle, D., and R. Widmer-Schmidrig (2008). The horizontal hum of the earth: A global background of spheroidal and toroidal modes, *Geophys. Res. Lett.* **35**, L06304, doi: [10.1029/2007GL033125](https://doi.org/10.1029/2007GL033125).
- Le Maistre, S., A. Rivoldini, A. Caldiero, M. Yseboodt, R.-M. Baland, M. Beuthe, T. Van Hoolst, V. Dehant, W. M. Folkner, D. Buccino, *et al.* (2023). Spin state and deep interior structure of Mars from InSight radio tracking, *Nature* **619**, no. 7971, 733–737.
- Li, J., C. Beghein, P. Lognonné, S. M. McLennan, M. A. Wiczorek, M. P. Panning, B. Knapmeyer-Endrun, P. Davis, and W. B. Banerdt (2023). Different Martian crustal seismic velocities across the dichotomy boundary from multi-orbiting surface waves, *Geophys. Res. Lett.* **50**, no. 1, e2022GL101243, doi: [10.1029/2022GL101243](https://doi.org/10.1029/2022GL101243).
- Lognonné, P., and C. Johnson (2015). 10.03—Planetary seismology, in *Treatise on Geophysics*, G. Schubert (Editor), Second Ed., Elsevier, Oxford, 65–120.
- Lognonné, P., W. Banerdt, J. Clinton, R. Garcia, D. Giardini, B. Knapmeyer-Endrun, M. Panning, and W. Pike (2023). Mars seismology, *Annu. Rev. Earth Planet. Sci.* **51**, 643–670.
- Lognonné, P., W. Banerdt, D. Giardini, W. Pike, U. Christensen, P. Laudet, S. de Raucourt, P. Zweifel, S. Calcutt, M. Bierwirth, *et al.* (2019). SEIS: Insight’s seismic experiment for internal structure of Mars, *Space Sci. Rev.* **215**, no. 1, 12, doi: [10.1007/s11214-018-0574-6](https://doi.org/10.1007/s11214-018-0574-6).
- Lognonné, P., W. Banerdt, W. Pike, D. Giardini, U. Christensen, R. Garcia, T. Kawamura, S. Kedar, B. Knapmeyer-Endrun, L. Margerin, *et al.* (2020). Constraints on the shallow elastic and anelastic structure of Mars from InSight seismic data, *Nature Geosci.* **13**, 213–220.
- Lognonné, P., J. G. Beyneix, W. B. Banerdt, S. Cacho, J. F. Karczewski, and M. Morand (1996). Ultra broad band seismology on InterMarsNet, *Planet. Space Sci.* **44**, 1237, doi: [10.1016/S0032-0633\(96\)00083-9](https://doi.org/10.1016/S0032-0633(96)00083-9).
- Lognonné, P., F. Karakostas, L. Rolland, and Y. Nishikawa (2016). Modeling of atmospheric-coupled Rayleigh waves on planets with atmosphere: From Earth observation to Mars and Venus perspectives, *J. Acoust. Soc. Am.* **140**, no. 2, 1447–1468.
- Lognonné, P., M. Schimmel, E. Stutzmann, P. Davis, M. Drilleau, G. Sainton, T. Kawamura, M. P. Panning, and W. B. Banerdt (2023). Detection of mars normal modes from s1222a event and seismic hum, *Geophys. Res. Lett.* **50**, no. 12, e2023GL103205, doi: [10.1029/2023GL103205](https://doi.org/10.1029/2023GL103205).
- Montalbetti, J. F., and E. R. Kanasevich (1970). Enhancement of teleseismic body phases with a polarization filter, *Geophys. J. Int.* **21**, no. 2, 119–129.
- Muirhead, K. (1968). Eliminating false alarms when detecting seismic events automatically, *Nature* **217**, no. 5128, 533–534.
- Nakamura, Y., and D. L. Anderson (1979). Martian wind activity detected by a seismometer at viking lander 2 site, *Geophys. Res. Lett.* **6**, no. 6, 499–502.
- Nawa, K., N. Suda, Y. Fukao, T. Sato, Y. Aoyama, and K. Shibuya (1998). Incessant excitation of the earth’s free oscillations, *Earth Planets Space* **50**, no. 1, 3–8.
- Nishida, K. (2013). Earth’s background free oscillations, *Annu. Rev. Earth Planet. Sci.* **41**, no. 1, 719–740.
- Nishida, K. (2014). Source spectra of seismic hum, *Geophys. J. Int.* **199**, no. 1, 416–429.
- Nishida, K., N. Kobayashi, and Y. Fukao (2000). Resonant oscillations between the solid earth and the atmosphere, *Science* **287**, no. 5461, 2244–2246.
- Nishida, K., J.-P. Montagner, and H. Kawakatsu (2009). Global surface wave tomography using seismic hum, *Science* **326**, no. 5949, 112–112.
- Nishikawa, Y., P. Lognonné, T. Kawamura, A. Spiga, E. Stutzmann, M. Schimmel, T. Bertrand, F. Forget, and K. Kurita (2019). Mars’ background free oscillations, *Space Sci. Rev.* **215**, 1–26.
- Okal, E. A., and D. L. Anderson (1978). Theoretical models for mars and their seismic properties, *Icarus* **33**, no. 3, 514–528.
- Panning, M. P., P. Lognonné, W. Bruce Banerdt, R. Garcia, M. Golombek, S. Kedar, B. Knapmeyer-Endrun, A. Mocquet, N. A. Teanby, J. Tromp, *et al.* (2017). Planned products of the Mars structure service for the InSight mission to Mars, *Space Sci. Rev.* **211**, 611–650.
- Pinot, B., D. Mimoun, N. Murdoch, K. Onodera, C. Johnson, A. Mittelholz, M. Drilleau, A. Stott, L. Pou, S. de Raucourt, *et al.* (2024). The InSitu evaluation of the SEIS noise model, *Space Sci. Rev.* **220**, 1572–9672.

- Posiolova, L. V., P. Lognonné, W. B. Banerdt, J. Clinton, G. S. Collins, T. Kawamura, S. Ceylan, I. J. Daubar, B. Fernando, M. Froment, *et al.* (2022). Largest recent impact craters on mars: Orbital imaging and surface seismic co-investigation, *Science* **378**, no. 6618, 412–417.
- Prieto, G. A. (2022). The multitaper spectrum analysis package in Python, *Seismol. Res. Lett.* **93**, no. 3, 1922–1929.
- Rhie, J., and B. Romanowicz (2004). Excitation of earth's continuous free oscillations by atmosphere–ocean–seafloor coupling, *Nature* **431**, no. 7008, 552–556.
- Richards, M. A., and C. W. Wicks Jr. (1990). S-P conversions from the transition zone beneath Tonga and the nature of the 670 km discontinuity, *Geophys. J. Int.* **101**, no. 1, 1–35, doi: [10.1111/j.1365-246X.1990.tb00755.x](https://doi.org/10.1111/j.1365-246X.1990.tb00755.x).
- Samson, J., and J. Olson (1980). Some comments on the descriptions of the polarization states of waves, *Geophys. J. Int.* **61**, no. 1, 115–129.
- Samuel, H., M. Drilleau, A. Rivoldini, Z. Xu, Q. Huang, R. F. Garcia, V. Lekić, J. C. Irving, J. Badro, P. H. Lognonné, *et al.* (2023). Geophysical evidence for an enriched molten silicate layer above Mars's core, *Nature* **622**, no. 7984, 712–717.
- Schimmel, M. (1999). Phase cross-correlations: Design, comparisons, and applications, *Bull. Seismol. Soc. Am.* **89**, no. 5, 1366–1378.
- Schimmel, M., and J. Gallart (2005). The inverse S-transform in filters with time-frequency localization, *IEEE Trans. Signal Process.* **53**, no. 11, 4417–4422.
- Schimmel, M., and H. Paulssen (1997). Noise reduction and detection of weak, coherent signals through phase-weighted stacks, *Geophys. J. Int.* **130**, 497–505.
- Schimmel, M., E. Stutzmann, and S. Ventosa (2018). Low-frequency ambient noise autocorrelations: Waveforms and normal modes, *Seismol. Res. Lett.* **89**, no. 4, 1488–1496.
- Scholz, J.-R., R. Widmer-Schmidrig, P. Davis, P. Lognonné, B. Pinot, R. F. Garcia, K. Hurst, L. Pou, F. Nimmo, S. Barkaoui, *et al.* (2020). Detection, analysis and removal of glitches from InSight's seismic data from Mars, *Earth Space Sci.* **7**, no. 11, e2020EA001317-T, doi: [10.1029/2020EA001317](https://doi.org/10.1029/2020EA001317).
- Snieder, R. (2004). Extracting the Green's function from the correlation of coda waves: A derivation based on stationary phase, *Phys. Rev. E* **69**, doi: [10.1103/PhysRevE.69.046610](https://doi.org/10.1103/PhysRevE.69.046610).
- Sollberger, D. (2023). solldavid/twistpy: Twistpy—First release (v0.0.1-beta), *Zenodo*.
- Stähler, S. C., A. Khan, W. B. Banerdt, P. Lognonné, D. Giardini, S. Ceylan, M. Drilleau, A. C. Duran, R. F. Garcia, Q. Huang, *et al.* (2021). Seismic detection of the Martian core, *Science* **373**, no. 6553, 443–448.
- Stähler, S. C., A. Mittelholz, C. Perrin, T. Kawamura, D. Kim, M. Knapmeyer, G. Zenhäusern, J. Clinton, D. Giardini, P. Lognonné, *et al.* (2022). Tectonics of Cerberus Fossae unveiled by marsquakes, *Nat. Astron.* **6**, no. 12, 1376–1386.
- Suda, N., K. Nawa, and Y. Fukao (1998). Earth's background free oscillations, *Science* **279**, no. 5359, 2089–2091.
- Tanimoto, T. (2001). Continuous free oscillations: Atmosphere-solid earth coupling, *Annu. Rev. Earth Planet. Sci.* **29**, 563–584.
- Tanimoto, T., and J. Um (1999). Cause of continuous oscillations of the earth, *J. Geophys. Res.* **104**, no. B12, 28,723–28,739.
- Tanimoto, T., S. Ishimaru, and C. Alvizuri (2006). Seasonality in particle motion of microseisms, *Geophys. J. Int.* **166**, no. 1, 253–266.
- Tanimoto, T., J. Um, K. Nishida, and N. Kobayashi (1998). Earth's continuous oscillations observed on seismically quiet days, *Geophys. Res. Lett.* **25**, no. 10, 1553–1556.
- Thomson, D. (1982). Spectrum estimation and harmonic analysis, *Proc. IEEE* **70**, no. 9, 1055–1096.
- Virtanen, P., R. Gommers, T. E. Oliphant, M. Haberland, T. Reddy, D. Cournapeau, E. Burovski, P. Peterson, W. Weckesser, J. Bright, *et al.* (2020). SciPy 1.0: Fundamental algorithms for scientific computing in Python, *Nat. Methods* **17**, 261–272.
- Wang, S., and H. Tkalčić (2022). Scanning for planetary cores with single-receiver intersource correlations, *Nat. Astron.* **6**, no. 11, 1272–1279.
- Wang, X., L. Chen, and X. Wang (2023). Renewed epicentral distribution of low frequency marsquakes by varying-parameter polarization analysis of insight data, *Geophys. Res. Lett.* **50**, no. 16, e2023GL103896, doi: [10.1029/2023GL103896](https://doi.org/10.1029/2023GL103896).
- Webb, S. C. (2007). The earth's 'hum' is driven by ocean waves over the continental shelves. *Nature* **445**, no. 7129, 754–756.
- Xu, W., Q. Zhu, and L. Zhao (2022). GlitchNet: A Glitch detection and removal system for SEIS records based on deep learning, *Seismol. Res. Lett.* **93**, no. 5, 2804–2817.
- Zenhäusern, G., S. C. Stähler, J. F. Clinton, D. Giardini, S. Ceylan, and R. F. Garcia (2022). Low-frequency marsquakes and where to find them: Back Azimuth determination using a polarization analysis approach, *Bull. Seismol. Soc. Am.* **112**, no. 4, 1787–1805.
- Zharkov, V., T. Gudkova, and A. Batov (2017). On estimating the dissipative factor of the Martian interior, *Sol. Syst. Res.* **51**, 479–490.
- Zheng, Y., F. Nimmo, and T. Lay (2015). Seismological implications of a lithospheric low seismic velocity zone in mars, *Phys. Earth Planet. In.* **240**, 132–141.

Manuscript received 29 April 2024

Published online 31 October 2024